Vibration and Crack Detection in Gas Turbine Engine Compressor Blades using Eddy Current Sensors

by

Matthew Lackner

B.S.E., Mechanical and Aerospace Engineering, Princeton University (2002)

SUBMITTED TO THE DEPARTMENT OF AERONAUTICS AND
ASTRONAUTICS IN PARTIAL FULFILLMENT FOR THE DEGREE OF

MASTER OF SCIENCE IN AERONAUTICS AND ASTRONAUTICS
AT THE
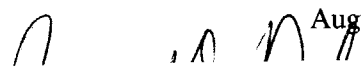MASSACHUSETTS INSTITUTE OF TECHNOLOGY

AUGUST 2004
[September 2004]

Signature of Author . . . .

Department of Aeronautics and Astronautics

August 20, 2004

Certified by . . . .

James D. Paduano

Principal Research Engineer of Aeronautics and Astronautics

Thesis Supervisor

Accepted by . . . .
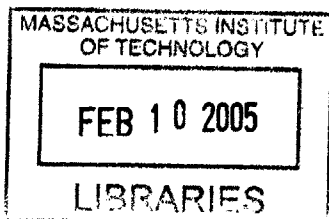
Jaime Peraire

Professor of Aeronautics and Astronautics

Chair, Committee on Graduate Students

1

Vibration and Crack Detection in Gas Turbine Engine Compressor Blades using Eddy Current Sensors

by

Matthew Lackner

Abstract

High cycle fatigue (HCF) cracks generated by compressor blade vibrations are a common source of failure in gas turbine engines. Current methods for crack detection are costly, time consuming, and prone to errors. In-situ blade vibration detection would help operators avoid critical engine speeds, and help infer the presence of cracks via a change in the mode of a blade. Blade vibrations can be detected using non-contacting sensors like optical sensors, or contacting sensors like strain gauges. These methods have drawbacks that make them poorly suited for installation in a gas turbine engine.

Eddy Current Sensors (ECS) have numerous advantages over other vibration detection methods. This thesis aims to use ECS's for vibration detection. Testing was performed in a spin pit rig in the Gas Turbine Lab at the Massachusetts Institute of Technology. The rig contained a rotor on which three test blades spun, and strain gauge and ECS data were extracted from the rig. Magnet arrays were used to provide an excitation force to the blades, causing them to vibrate as they were spinning.

Force hammer testing was used to determine the resonant frequencies and mode shapes of the test blades, as well as transfer functions from the strain gauges to the blade tip acceleration. These transfer functions allowed for independent knowledge of the blade vibration behavior. The case of a cracked blade was also considered. Estimates were performed to determine the proper location and length of a crack in the test blade. A 10 mm edge crack was created in a test blade. The crack was found to lower the resonant frequency of the first torsion mode of the blade by 0.2%, and to alter the transfer function between strain and tip acceleration. While some evidence of the blade vibration appears in the ECS signal, no definitive method for sensing blade vibration using an ECS has yet been developed.

Thesis Supervisor: Dr. James D. Paduano
Title: Principle Research Engineer, Department of Aeronautics and Aeronautics

Acknowledgements

First, I would like to thank my advisor Dr. James Paduano. He was a steady source of guidance, direction, and wisdom, and I greatly appreciate all his help.

Second, thanks to all the people in the GTL who assisted me along the way. Jimmy Letendre, Jack Costa, Victor Dubrowski, Gerald Guenette, Yiben Lin, Headley Jacobus, George Zipfel, and John Kane all were instrumental in helping me complete my work.

Also, thank you Technosciences, Inc. for sponsoring this work.

Lastly, thanks to my family, friends, and my girlfriend Julie for their support and patience throughout my time at MIT.

Table of Contents

6

List of Figures

List of Tables

1 Introduction

1.1 Compressor Blade Vibrations and Cracks

Compressor blade vibrations in a gas turbine engine are an important problem. Vibrations can lead to non-ideal aerodynamic performance of the blades. More importantly, excessive blade vibration can cause stresses in a blade that can lead to high cycle fatigue (HCF) failure. HCF failure is caused by cyclic stresses that lead to crack initiation and growth, and eventually to failure. HCF is distinguished from low cycle fatigue (LCF) by the stress level. HCF is due to stress levels that are well below the yield stress, causing solely elastic deformations of the material, and therefore requiring a high number of cycles to bring about failure.[1] In fact, HCF is one of the most common causes of failure in gas turbine engines. The high occurrence of HCF failures can be seen in Figure 1.1
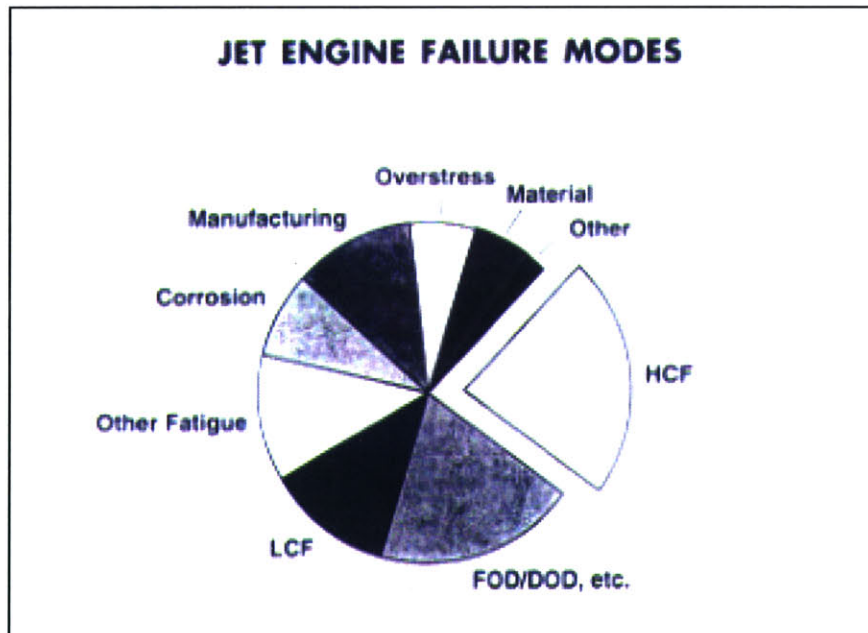
Figure 1.1: HCF Failure Percentage[2]

HCF failures occur during both development and engine operation, and can lead to catastrophic events. A HCF crack that causes a blade to break off of the disk can damage an engine severely enough to bring down the entire airplane. The 1989 crash of United

11

Airline flight 232 killed 111 people, and was initiated by an undetected HCF crack in an engine.[3] It is clear that blade vibrations, which can lead to HCF failures, are a significant problem in gas turbine engines.

1.1.1 Compressor Blade Modes

Like all structures, compressor blades have resonant modes and corresponding resonant frequencies. A mode is the shape that the structure deforms to when it vibrates at the resonant frequency. A guitar string pinned at the ends, with the center vibrating transversely is a simple example of a mode. Compressor blades can be modeled as simple cantilever beams, with associated bending and torsion modes, as seen in Figure 1.2. For higher frequency modes, the shapes become more complex.
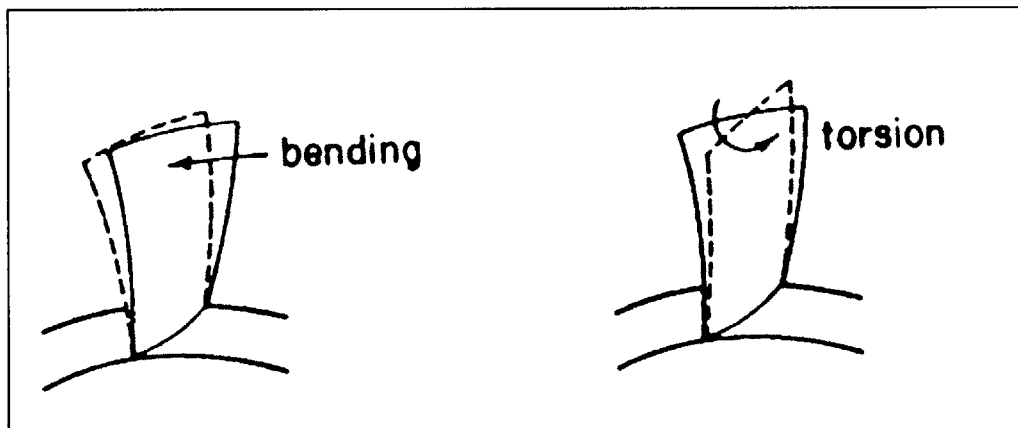
Figure 1.2: Compressor Blade Mode Shapes[4]

When compressor blade modes are excited, the blade will vibrate, and these vibrations can cause HCF cracks, as stated above. A particular mode of a compressor blade will be excited when the resonant frequency is an integral multiple of the engine rotation speed. For example, a mode at 1000 Hz will be excited when the engine rotation speed is 1000 Hz, 500 Hz, 333 Hz, etc. This relationship can be demonstrated visually using a "Campbell diagram." An example of a Campbell diagram is shown in Figure 1.3. The horizontal lines represent the resonant frequencies of the blade – in this case they correspond to the first two bending modes. The diagonal lines have slopes that are

integral multiples of the engine rotation speed i.e. N, 2N, 3N, etc. The points where the diagonal engine speed lines intersect the horizontal resonant frequency lines indicate the critical engine speeds that can cause the modes of the blades to be excited. Thus, when an engine operates at a critical speed, one of the blade modes will be excited, and the blade will vibrate. The longer an engine resides at a critical speed, the more fully the blade mode becomes excited, and so the stress levels increase.
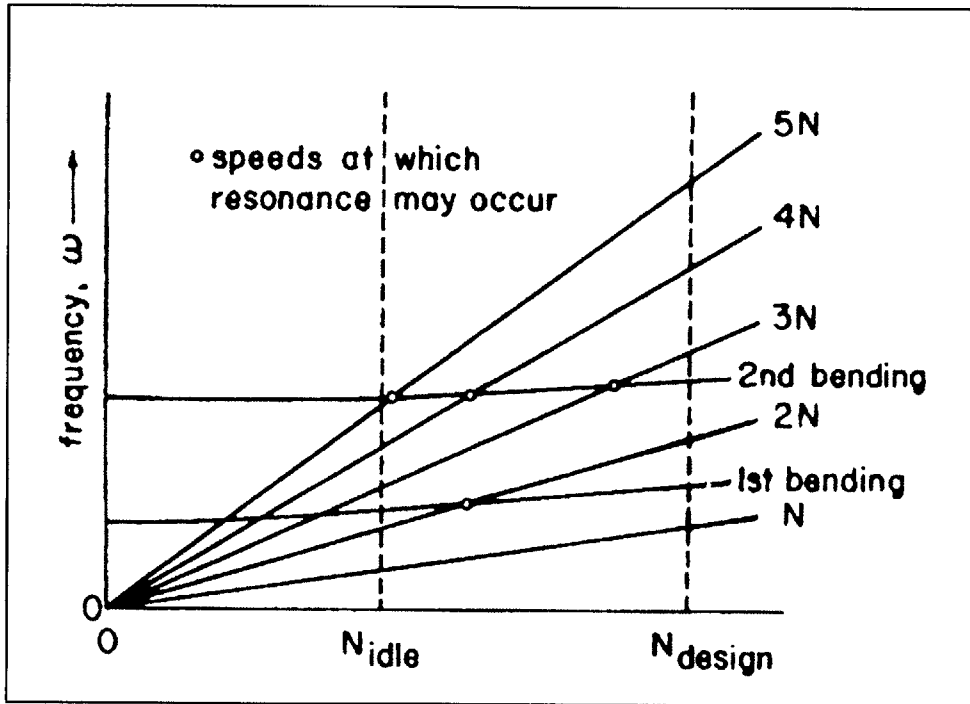
Figure 1.3: Sample Campbell Diagram [4]

1.1.2 Blade Cracks

Vibrations cyclically stress blades, and this cyclic loading can lead to HCF cracks. HCF cracks consist of three distinct steps. First, the crack must initiate. In this step, the cyclic loading causes a small crack to form, usually in a region of stress concentration. Next, the crack propagates, advancing incrementally with each cycle.[1] Finally, the structure fails, as the crack grows rapidly after reaching a critical size. The total number of cycles to failure is just the sum of the number of cycles needed for initiation and the number of cycles needed for propagation; the number of cycles contributing to failure is

13

insignificant. For the low stress levels associated with HCF, the number of cycles required for initiation is greater than propagation.

Currently, there are several methods for blade crack detection, all of which require the engine to be removed from the airplane and disassembled for periodic inspection. One such method is fluorescent penetrant inspection (FPI).[5] Blades are coated with dye that seeps into cracks, which can then be seen under ultraviolet light. However, FPI cannot detect subsurface cracks. Ultrasonic and eddy current probes can also be used for crack detection. All of these crack detection methods have several drawbacks. First, removing and disassembling an engine is a time consuming and expensive process. Second, when the testing occurs, blades are in their most relaxed states, and therefore cracks are smallest and more difficult to detect.[5] Lastly, all of these methods require an experienced operator, and are subject to human error. To minimize the possibility for blade failure, disks are retired after substantially fewer cycles than would be expected to cause crack initiation. Despite this precaution, blade failures do occur when cracked blades go undetected. The result is that most blades are retired well before their lifetime is up, while a small number of blades fail and cause significant damage.[5] The entire process is extremely costly, as many useful blades are wasted, some bad blades cause engine failure, and many hours are spent disassembling and inspecting the engine.

Currently, no method exists for detecting cracks in-situ. Such a system, imbedded in an engine, would have the benefit of eliminating the need for the engine to be removed and disassembled. This would lead to substantial cost savings. Moreover, an in-situ system would detect cracks while the blades are at a high stress level, and so the cracks are largest, and easier to detect. Obviously, there is substantial motivation to develop an in-situ crack detection method.

1.1.3 Vibration Sensing

There are many existing techniques for blade vibration sensing. However none of these methods are well suited for operation in gas turbine engines. Strain gauges are a well-

known method for vibration sensing. However, strain gauges take time to install, and are prone to failure. They are far too fragile to withstand the gas turbine environment. Blade vibrations can also be detected using non-contacting sensors, like optical or capacitive sensors. These sensors use time of arrival data to sense blade vibrations. That is, they measure the time at which the rotating blade tip passes a stationary sensor to determine the vibration of the blades. A major drawback of this method is that it requires several sensors to determine blade vibrations, usually at least four. This requirement for a large number of sensors in each stage of an engine can make the cost of vibration sensing prohibitive. Finally, optical and capacitive sensors tend to be heavy and expensive, and are adversely affected by the extreme environment of a gas turbine engine. Gas turbine engines are extremely high temperature environments with high vibration levels, and conventional non-contacting sensors are poorly suited for these conditions.

Sensing blade vibrations while an engine is in operation is potentially very useful. First, if blade vibrations could be detected, this knowledge would indicate critical engines speeds that could be avoided in the future. Second, vibration sensing could be used for crack detection. Cracks change the structural properties of a blade. This change in the structural stiffness would alter the mode shape and frequency of a blade. Thus, if blade vibrations can be sensed, then the presence of a crack can be inferred due to a change in the mode shape and frequency of a blade.

1.1.4 Overview of Blade Vibrations and Cracks

There is a clear and compelling motivation to sense blade vibrations in gas turbine engines. Blade vibrations lead to high cycle fatigue cracks, which can cause catastrophic engine failure. Currently, blade vibrations can be detected using strain gauges or non-contacting time of arrival methods. These methods have drawback ranging from reliability to cost. The ability to sense blade vibrations would identify critical engine speeds and potentially allow for crack detection. Current methods for crack detection are expensive and subject to errors. In sum, the ability to sense blade vibrations in operating gas turbine engines could improve safety and reduce maintenance costs.

1.2 Eddy Current Sensors

This thesis focuses on using eddy current sensors (ECS) for blade vibration sensing. As discussed in Section 1.1.3, current methods for vibration sensing have numerous drawbacks. Eddy current sensors have the possibility to mitigate these drawbacks, and could be used for vibration sensing in an operating gas turbine engine.

This thesis will utilize an ECS developed by General Dynamics Advanced Technology Systems (GDATS). The GDATS ECS was developed for the Joint Strike Fighter (JSF) program.[3] Currently, the GDATS ECS is being used only for tip clearance detection in the JSF, and not for vibration sensing. Technosciences Inc., the sponsors of this thesis, intends to use the ECS to sense blade vibrations using only two sensors. They are developing algorithms to utilize the full ECS signature for vibration sensing, rather than using time of arrival methods, mentioned in Section 1.1.3, which requires at least four sensors to sense vibrations.

1.2.1 Eddy Current Sensor Basics

Eddy current sensors operate by producing a time varying magnetic field. When a conducting object, e.g. a compressor blade, enters the field of the sensor, eddy currents are created in the conducting object. These eddy currents alter the magnetic field of the sensor, and the sensor measures this change in the field. The behavior of an eddy current sensor can be seen in Figure 1.4.
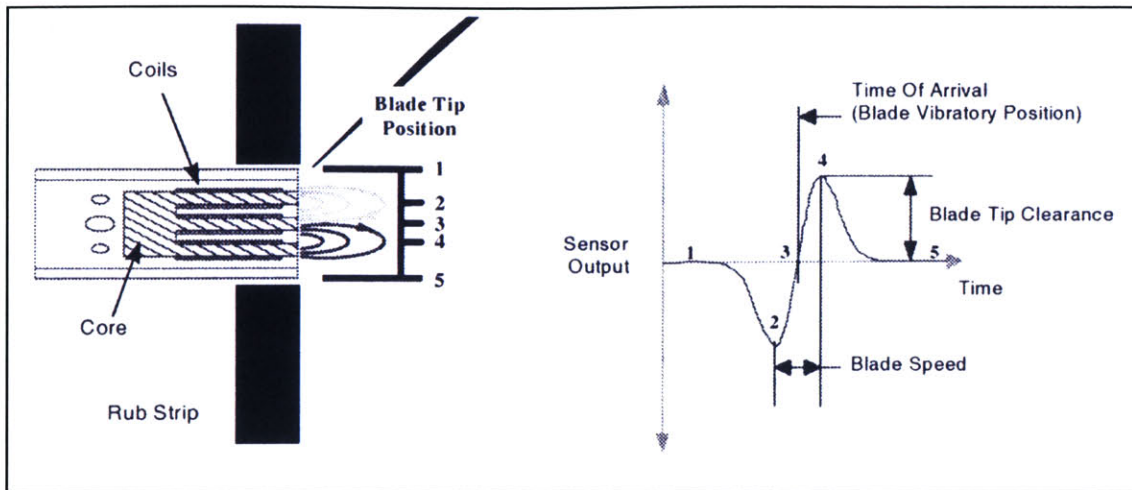
Figure 1.4: Eddy Current Sensor Output[3]

The picture on the left shows a blade passing the face of an eddy current sensor at various positions. The picture on the right shows the corresponding voltage output of the sensor. Several important characteristics of the output are shown in the picture on the right. First, when the blade passes the center of the sensor at position 3, the eddy current sensor signature crosses zero. This zero crossing point can be used to calculate the time of arrival of a blade. Second, the peak-to-peak amplitude of the eddy current sensor signature is proportional to the tip clearance. As mentioned above, the ECS is currently used for tip clearance measurements in the JSF program. Third, the speed of the passing blade is proportional to the peak-to-peak width of the ECS signature.

1.2.2   Advantages of Eddy Current Sensors

ECS's have many properties that make them well suited for installation in an operating gas turbine engine, and a superior choice to other vibration sensing technologies. First, they are simply constructed and low in cost relative to optical sensors. Second, they are small, light, and durable.[3] They can withstand the high temperatures and accelerations of a gas turbine engine environment. Moreover, they can operate without any cooling. Third, an ECS is immune to dirt and moisture in the gas stream, which is not the case for optical and capacitive sensors. Overall, they are well suited for permanent installation in a gas turbine engine.

17

1.2.3 Goals

The long-term goal of the proponents of this technology is for ECS systems to become permanently installed sensor systems in gas turbine engines. These casing mounted systems would sense blade vibrations and potentially identify crack growth in blades. As stated in Section 1.1.4, there is a strong motivation to sense blade vibrations and the presence of cracks both from the perspective of safety and cost. Compared to other vibration sensing technologies, an ECS system offers many advantages in terms of cost and reliability.

For this thesis, the research performed aimed to fulfill several specific objectives.

1. Utilize magnet arrays to cause a spinning blade to vibrate. Determine to what degree the magnets caused vibrations and verify that these vibrations can be identified using strain gauges.

2. Determine the mode shapes of a blade, and generated transfer functions relating the strain gauge signal to the blade tip behavior.

3. Resolve the following question: How much does a crack affect the mode of a blade? How should a blade be cracked to make the situation as realistic as possible?

4. Identify blade vibrations in the ECS signals.

1.3 Overview of Thesis

This thesis consists of experimental work performed in the spin pit rig in the Gas Turbine Lab (GTL) at the Massachusetts Institute of Technology (MIT). Broadly, test blades were spun in the spin pit to simulate a rotating engine. Magnet arrays were used to provide forces to excite the modes of the blades. Strain gauges were installed on the blades to provide independent measurements of the blade behavior. Eddy current sensors were mounted around the circumference of the spin pit, and ECS data was taken while the blades were rotating. ECS data was then analyzed in conjunction with strain gauge data to identify blade vibrations. The basic structure of the thesis proceeds as follows:

18

- Chapter 2 describes the experimental setup for the testing, including the creation of the test blade, the spin pit, the strain gauges, the magnet arrays, and the data acquisition system.

- Chapter 3 describes the experimental procedure and preliminary data collection and analysis. Force hammer testing and analysis, finite element analysis, rotor balancing, and blade excitation are all discussed.

- Chapter 4 focuses on analysis of the ECS data and estimates of the size and effect of a high cycle fatigue crack on blade modes.

- Chapter 5 discusses the conclusions reached from the analysis, and some recommendations for future work.

2 Experimental Setup

2.1 Spin Pit Rig

Experimental work for this thesis was conducted in the spin pit rig, located in the Gas Turbine Lab at the Massachusetts Institute of Technology. The rig consists of a rotor located within a 30-inch diameter and 7-inch deep steel cylinder. The rotor has three hub mounts that are used to mount blades. A picture of the rig is shown in Figure 2.1. The lid of the spin pit has been removed to show the rotor, as well as three blades mounted in the rotor.
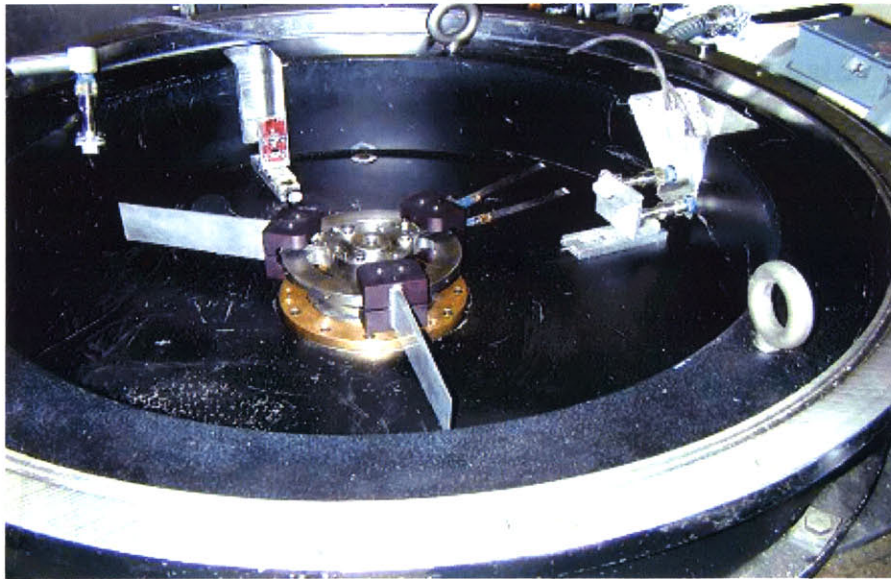
Figure 2.1: Spin Pit Rig

A motor drives the rotor, which is capable of spinning the rotor up to 300 Hz (18,000 RPM). The spin pit can be sealed and evacuated with a vacuum pump in order to reduce the aerodynamic drag on the rotating blades. Thermocouples are mounted on the rotor bearings to ensure that the temperature from frictional heating remains in an acceptable range. The dynamic vibrations of the rotor are measured with an accelerometer located in the housing of one of the rotor bearings.

Both stationary and rotating frame data can be extracted from the spin pit rig. Two brackets have been installed around the circumference of the rig for the eddy current sensors. These brackets are mounted on traversers that can be adjusted to position the eddy current sensors at a desired distance from the rotating blade tips. The brackets can be seen in Figure 2.1. The eddy current sensor output is extracted through a cable, which passes through a vacuum seal in the lid of the spin pit, to a signal-conditioning box. Data from the strain gauges mounted on the rotating blades can also be extracted from the rig. The strain gauge output passes through a slip ring located at the top of the rotor, and emerges through wires that are connected to the strain gauge amplifiers.

2.2 Test Blade Creation

A blade was created for the spin pit testing. The test blade profile started as a Matlab description of the 'Fan C' transonic fan blade designed by GE. The profile contained x-y coordinate cross-sections of the blade at nine different span-wise locations. A picture of the original blade is shown in Figure 2.2.
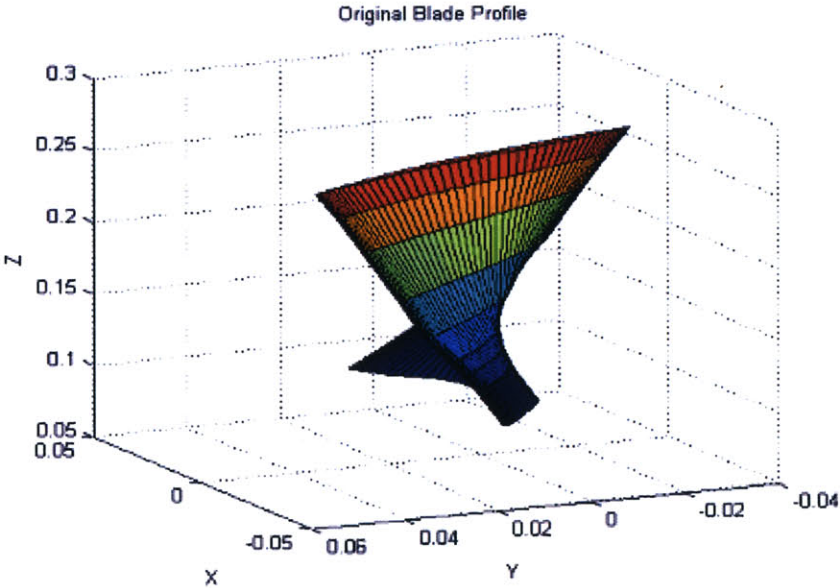
Figure 2.2: Original Fan-C Blade Profile in Matlab

For each of the cross-sections, the twist and the camber were removed, so that the description represents the thickness profile of a real blade, with twist and camber

removed. The blade was then scaled down in size by normalizing the chord length of each cross section to 2 inches to fit into the hubs of the test rotor. This easily manufactured blade has a realistic taper ratio and thickness at each radial station, but is much easier to analyze and test.

Next, the modified blade profile was imported into Pro Engineer, creating a three dimensional representation with a simple 'fir tree' at the hub to secure the blade in the spin pit rotor hub. A picture of the blade in 'Pro-E' appears in Figure 2.3.
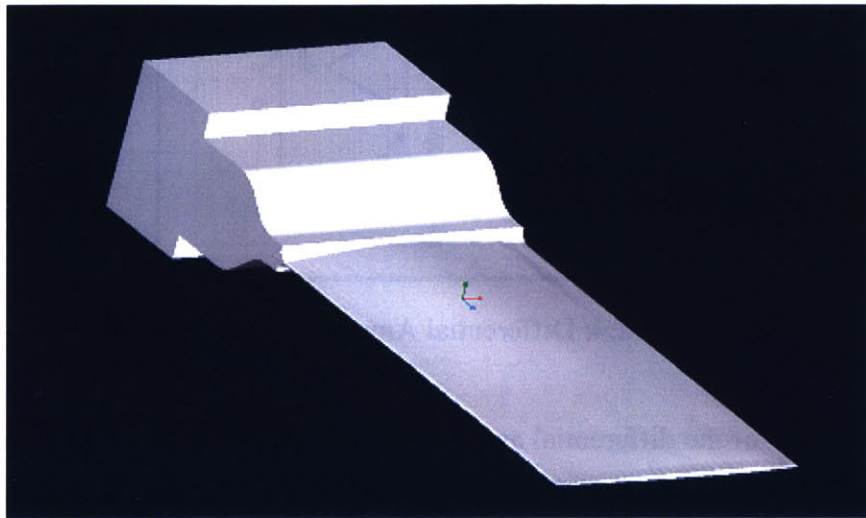
Figure 2.3: Pro Engineer Representation of Test Blade

Finally, manufacturing files were created so that the blade could be manufactured in the 5-axis milling machine in the Gas Turbine Lab machine shop. To date, six blades have been manufactured from aluminum.

2.3 Eddy Current Sensors

Three eddy current sensors have been mounted in the spin pit at various circumferential and chord wise locations. Two sensors are mounted on a single traverser – one at 25% of the chord, one at 75% of the chord of the blades. The third sensor is mounted on a separate traverser, 90 degrees from the other sensors. This third sensor is positioned at 25% of the chord. The positions of the sensors can be seen in Figure 2.1. The sensor

output passes through a vacuum seal to a signal-conditioning box. The output of the signal-conditioning box is connected to a differential amplifier. The differential amplifier is unity gain, and is used for common mode rejection. A schematic of the differential amplifier is shown in Figure 2.4.
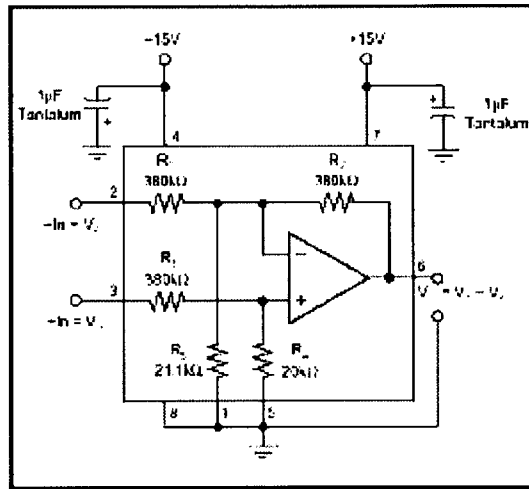
Figure 2.4: Differential Amplifier Schematic[6]

Finally the output of the differential amplifier connects to a BNC cable, so that the sensor output can be viewed on an oscilloscope or connected to the data acquisition equipment. The differential amplifier has been found to effectively reduce the noise level in the eddy current sensor signal.

2.4 Strain Gauges

2.4.1 Strain Gauge Positioning

Two blades were each wired with strain gauges in order to independently sense blade vibration. For one blade, four strain gauges were positioned to sense bending modes. On this blade, the four gauges are all positioned so that they are parallel with the leading and trailing edge of the blade. Two strain gauges are on one side of the blade, and the other two strain gauges are mirror images on the other side. The strain gauges are all positioned at approximately 1/3 of the span of the blade. Two of the gauges are at ¼ of

the chord, and two are at ¾ of the chord. The positions of each of the strain gauges are shown in the illustration in Figure 2.5. The strain gauges are highlighted in black, and the dashed line indicates flipping from one side of the blade to the other.
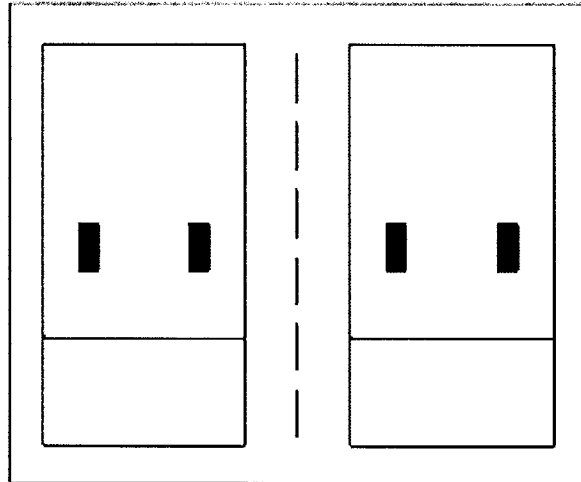
Figure 2.5: Strain Gauge Positions for Bending Blade

The strain gauges on the second blade were positioned to detect torsion modes. Once again four strain gauges were used, with two on each side mirroring those on the other side. The gauges are also at 1/3 the span and ¼ and ¾ of the chord. However, all four of the strain gauges are positioned at 45-degree angles to the leading and trailing edges. The positions of the strain gauges on the torsion blade are shown in Figure 2.6.
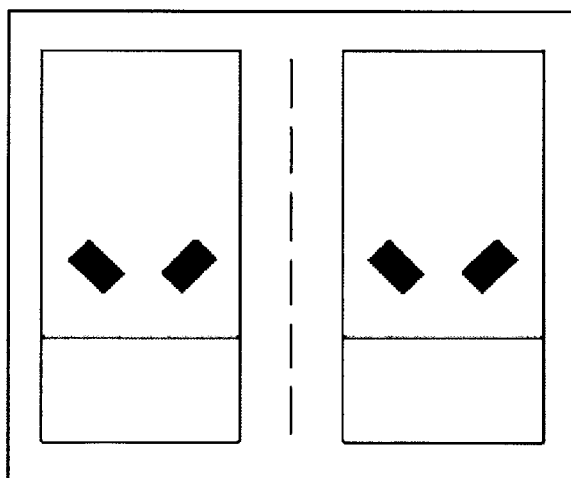
Figure 2.6: Strain Gauge Positions for Torsion Blade

2.4.2 Strain Gauge Wiring Scheme

The strain gauges for both blades were wired as a full Wheatstone bridge. A diagram of a Wheatstone bridge is shown in Figure 2.7. Each resistor represents one of the strain gauges.
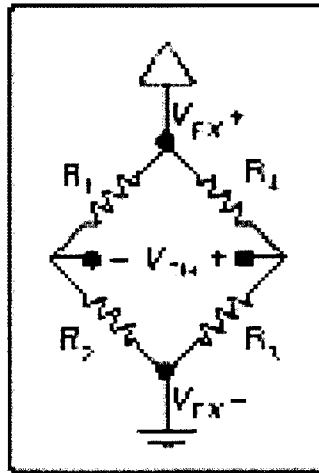
Figure 2.7: Wheatstone Bridge

For a full bridge, all four of the resistors correspond to each of strain gauges. When a strain gauge undergoes tension, the resistance of the strain gauge increases. Likewise, when it undergoes compression, the resistance decreases. The four strain gauges can be connected to each other in such a way that they make a full bridge. Consider the case of bending. When the blade bends, the two gauges on one side of the blade undergo a tension force, while the two gauges on the opposite side undergo a compressive force. V_EX is the excitation voltage, which is provided by the amplifier to power the bridge. If the gauges are wired such that the two gauges that experience tension are R1 and R3 in the Wheatstone bridge, and the two gauges that experience compression are R2 and R4 in the Wheatstone bridge, then a voltage will appear across V_CH. This voltage, V_CH, is the output voltage signal. A similar effect occurs for the torsion blade, but with a small difference. When a torsion blade twists, the strain gauges are affected differently. On one side of the blade, one gauge will experience a tension force. However, the force on the other gauge is perpendicular to the direction of the gauge. Consequently, that gauge experience only a slight compressive force, which is the tension force felt by the other

gauge, times the Poisson ratio of the material. On the other side of the blade, one of the gauges will experience a compressive force equal to the tension force felt by the gauge on the other side of the blade. The other gauge will experience a tension force equal to the small compressive force felt by the gauge on the other side of the blade. Although these changes in resistance are relatively small, they will result in a voltage signal, V_CH, to appear across the bridge.

A full bridge is an advantageous setup for the strain gauges for a variety of reasons. First, a full bridge eliminates centrifugal stress effects. When the blade is spun, centrifugal forces produce a tension force throughout the blade. However, all four strain gauges are at the same span-wise location, so they experience the same tension force. Since each gauge experiences the same stress, the resistance of each gauge increases the same amount. The result is that the bridge is unaffected by the centrifugal stress, and V_CH is zero. Thermal effects are canceled out in the same way. As a spinning blade heats up due to rotor and aerodynamic friction, the blade tends to lengthen somewhat. Again, all four of the gauges experience the same force, and so the output of the bridge is zero. Lastly, a full bridge greatly reduces the effect of noise in the slip ring. Originally, the strain gauges were wired as half bridges. Two strain gauges on the blade made up two of the resistors in the bridge, and the amplifier made up the other two resistors for a half bridge. The slip ring was in series with the strain gauges. While the resistance of the slip ring is nearly constant, it does vary slightly as the rotor spins. This small change in the slip ring resistance can introduce a great deal of noise. When the strain gauges experience some force, their resistance changes very slightly. When the variable resistance of the slip ring is included in the bridge, the actual signal becomes drowned out by the noise. However, when a full bridge is used, this effect is eliminated. For a full bridge, all four gauges in the bridge are on the blade. The signal that passes though the slip ring is the voltage signal V_CH. V_CH is connected to the amplifier, which is a very high impedance device, so that the small changes in resistance in the slip ring are negligible. Thus, a full bridge offers many advantages over other wiring schemes.

2.4.3 Strain Gauge Calibration and Output

In order to relate the strain gauge voltage output to the actual strain experienced by the gauges, the amplifier must be calibrated. The amplifier used was a Model 2310 Strain gauge Conditioning Amplifier from Measurements Group, INC. The method used to calibrate the amplifier is called "shunt" calibration. Both the bending and torsion blade were calibrated in this manner. The method proceeds as follows. A large resistor, a "shunt resistor," is placed in parallel with one of the strain gauges in the full bridge. The effect of the shunt resistor is to reduce the total resistance across the two resistors in parallel. Because the resistance of the shunt resistor is large compared to the strain gauge, the overall resistance is reduced only slightly. A decrease in resistance simulates a compressive strain on the gauge. In this way, a known strain can be simulated on one of the strain gauges, and the gain can be adjusted accordingly. The relation between the simulated strain and the shunt resistance is given in Equation 2.1.[7]

$$\varepsilon_{CAL} = \frac{R_A}{K(R_{CAL} + R_A)}$$

Equation 2.1

where: ε_{CAL} = simulated strain

K = gauge factor of the strain gauge

R_A = resistance of the shunted leg

R_{CAL} = resistance of the shunt resistor

The resistance of the shunted leg is just the resistance across the shunt resistor and the strain gauge in parallel, so:

$$\frac{1}{R_A} = \frac{1}{R_{SG}} + \frac{1}{R_{CAL}}$$

Equation 2.2

R_{SG} is just the resistance of the strain gauge, and the gauge factor is a known property of the strain gauge. Thus, if the resistance of the strain gauge and the shunt resistor are known, the simulated strain can be calculated. Then, the gain on the amplifier can be adjusted to produce a desired output. For this thesis, the amplifier was calibrated for a conversion factor of:

$$SG\_Conversion\_Factor = 520\frac{\mu\varepsilon}{V}$$

where $\mu\varepsilon$ is micro-strain, or strain divided by 10^6. This conversion factor applies to the whole bridge, so that each strain gauge actually experiences ¼ of the output. For example, an output of 10 V corresponds to a total strain of 5200 $\mu\varepsilon$, and a strain of 1300 $\mu\varepsilon$ per strain gauge. This conversion factor was chosen to achieve maximum sensitivity. The shunt resistor had a maximum resistance of 11,000 Ohms, which limits the amount of gain that is attainable. Also, this conversion factor applies to both the bending and the torsion blade. However, for the torsion blade, each gauge does not read simply ¼ of the total strain calculated. As stated in Section 2.4.2, two of the gauges experience the full force; the other two gauges experience this force times the Poisson Ratio. Thus, the strain felt by each gauge is not equal to the ¼ the total strain. If the Poisson Ratio is assumed to be small, then two of the gauges can be assumed to experience zero strain, while the other two each experience half the total strain. In general, this approximation will be used.

The output of the strain gauge amplifier is a simple voltage signal that can be connected to a BNC cable. The BNC cable can then be connected to an oscilloscope to view the strain output, or the data acquisition system to take strain gauge data.

2.5 Exciter Magnets

In order to sense vibrations, the test blade must be vibrating while the rig is spinning. An array of magnets is used to excite the modes of the blade while it rotates.

2.5.1 Magnet Positioning

Three sets of six samarium-cobalt magnets were positioned in the spin pit to provide an excitation to the blades. The magnets are each 1.0 x 0.5 x 0.25 inches in dimension. The three sets are positioned 120 degrees apart from each other, so that the forces they impart to the blades are balanced. Each holder for the set of magnets is bolted into the floor of

the spin pit. The holders consist of a ¾-inch thick steel plate, on top of which the magnets are positioned. The magnets are held in place by 1/16-inch dowel pins. Underneath the steel plate is a ¼-inch aluminum plate. Three jacking screws can be used to raise the steel plate above the aluminum plate to bring it closer to the blades. The magnets are positioned such that they lie on a circle centered at the axis of rotation of the rotor, at a radius that positions them at approximately half the span of the blades. A picture from Pro-Engineer of the magnets and the holder is shown in Figure 2.8. The picture does not show the aluminum plate or the holes, but it gives a good representation of the positioning of the magnets and the dowel pins.
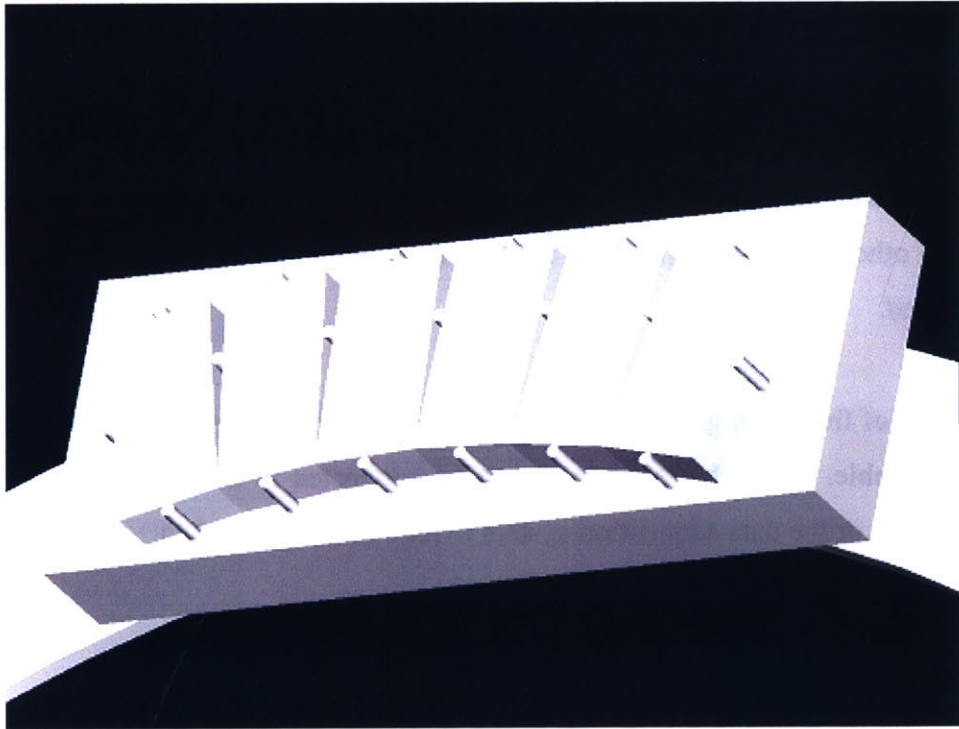
Figure 2.8: Magnet Layout and Holder

2.5.2 Magnet Physics

The magnets in the holder alternate in polarity. That is, each magnet has either a north or south pole facing upwards, and they alternate in which pole is facing upwards. Because of this positioning, the magnetic field above the magnet array is setup like a series of horseshoes, three per holder. As a blade passes through this magnetic field, eddy currents

are setup in the blade. According to Lenz's law, the eddy currents will be setup up so that they produce a magnetic field that opposes the change in magnetic flux in the blade. This effect results in a force on the blades. Thus, the magnets can be used to provide a periodic excitation to the blades as they rotate.

2.5.3 Magnet Excitation Frequency

The magnets will excite the blade at a certain frequency. This excitation frequency is dependent on the speed of the rotor and the angular separation of the magnets. The formula relating these parameters is:

$$F_{EX} = F_{ROT} * \frac{2\pi}{\Delta\theta}$$

Equation 2.4

where: F_{EX} = excitation frequency provided by the magnets in Hz.

F_{ROT} = rotational speed of the rotor in Hz.

$\Delta\theta$ = angular separation of the magnets

The angular separation of the magnets can be calculated geometrically. The inner two corners of each magnet are positioned so that they lie on a circle of radius 5.5 inches. The magnets are each 0.5 inches wide. Their angular separation was calculated using these values in Figure 2.9, with the result that $\Delta\theta$=5.2°.
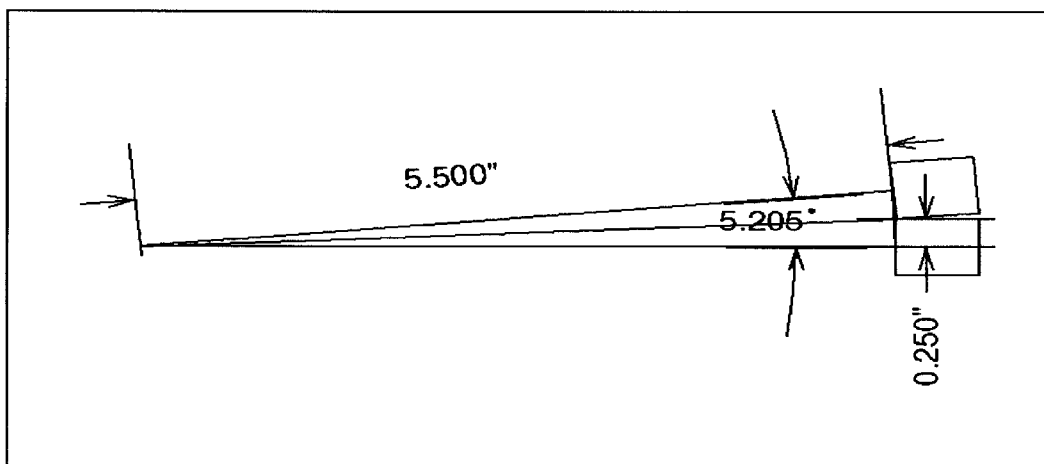
Figure 2.9: Angular Separation of Magnets

31

Thus, if the resonant frequencies of the blade are known, a certain frequency, F_{EX}, can be excited by running the rotor at the speed, F_{ROT}, given by Equation 2.4.

2.6 Data Acquisition

A "Lab View" program was developed that can read data through a National Instruments PCI-6071E A/D board. The strain gauge signals and the ECS signals can be measured simultaneously using the A/D board. The A/D board can take a total of 2 million samples per second. In general, data has been sampled at either 200 kHz or 400 kHz depending on the number of channels being used. Originally, the A/D board picked up noise produced by the spin pit motor. This problem was corrected by connecting the ground wires of each channel to the box, so that the shield became grounded. This change effectively eliminated the pickup of the rotor noise.

3   Experimental Procedure and Data Collection

3.1   Force Hammer Testing

The goal of this research is to sense vibrations of rotating blades using stationary eddy current sensors. In order to verify the accuracy of the eddy current sensors, it is important to have an independent source of measurement of the blade behavior that can serve as a "truth model." To that end, strain gauges are used to measure the blade vibrations while the rig is spinning. Strain gauge signals can be extracted through the spin pit slip ring, so that blade vibrations can be sensed simultaneously using both the eddy current sensors and the strain gauges. Because the ECS measures the blade behavior at the tip only, it is necessary to relate the strain reading at the location of a strain gauge to the blade tip behavior. In order to determine this relationship, an experiment was performed with the goal of determining the transfer function between the strain gauge reading, and the blade tip vibrations.

3.1.1 Force Hammer and Accelerometer

An impulse force hammer and an accelerometer were used to perform this experiment. The force hammer used was a Kistler model 9722A. Force hammers provide a structural excitation to the blade so that a frequency response function can be measured. Depending on the hammer tip selected, the hammer provides an input energy with nearly constant amplitude over the desired frequency range.[8] A Kistler model 8614A accelerometer was used to measure the blade vibrations. The force hammer and accelerometer were both connected to a digital signal analyzer, which produces a frequency response function for the accelerometer due to the force hammer input.

3.1.2 Resonant Frequency Determination

The force hammer, accelerometer, and strain gauges were first used to determine the resonant frequencies of both blades. The strain gauges on the "bending blade" were positioned to sense bending modes, while those on the "torsion blade" were positioned to sense torsion, as discussed in Section 2.4. Because the eddy current sensors are only about 1 inch in diameter, the blade is passing the sensor for only a small amount of time. However, this thesis proposes using the sensors to determine blade vibrations. Therefore it is necessary for the modes we are sensing to have resonant frequencies greater than 1000 Hz. This was the cutoff so that a significant portion of the mode period occurred within the window of the eddy current sensor. A sample frequency response function between the force hammer and accelerometer for the bending blade is shown in Figure 3.1. Two prominent peaks at 1208 Hz and 1284 Hz indicate the resonant frequencies of two different modes.
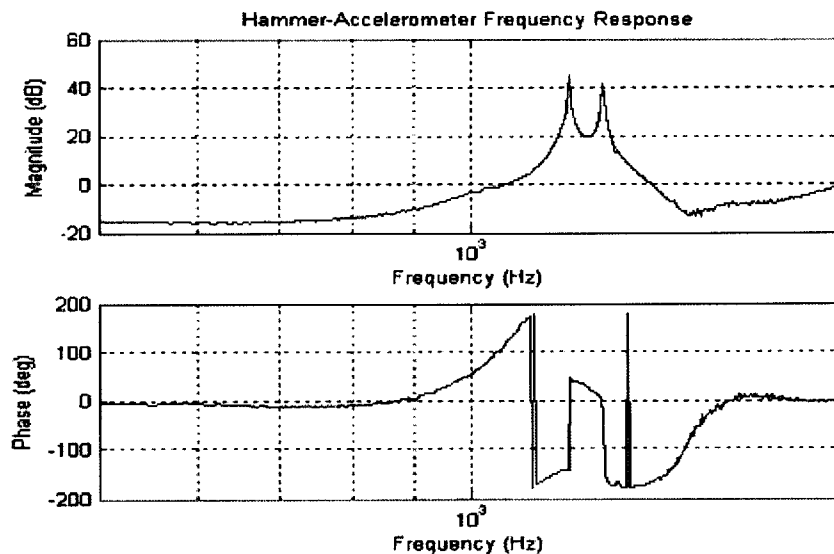
Figure 3.1: Impact Hammer to Accelerometer Frequency Response Function for Bending Blade

Similar tests were performed on the torsion blade as well. For the torsion blade, the resonant frequencies occurred at 1176 Hz and 1236 Hz. It seems that manufacturing

variations have caused the resonant frequencies to vary slightly between different blades. A summary of the resonant frequency determination appears in Table 3.1.

Bending Blade	Torsion Blade
1208 Hz	1176 Hz
1284 Hz	1236 Hz

Table 3.1: Summary of Resonant Frequency Determination

3.1.3 Mode Shape Determination

The next goal was mode shape determination. The mode shapes of the bending and torsion blade were both determined. Originally, it was intended that the accelerometer be placed at various locations along the blade tip, and then the blade would be struck with the force hammer, producing frequency response functions at each location. However, it was observed that the accelerometer's mass changed the inertia of the blade tip, causing the resonant frequencies to shift, depending on the location of the accelerometer. Therefore, an alternate method was used, in which the accelerometer remained positioned near the root of the blade, and near the leading edge, where it was conjectured that the effect of the mass would be small. The accelerometer position is shown in Figure 3.2, and is labeled x_a.
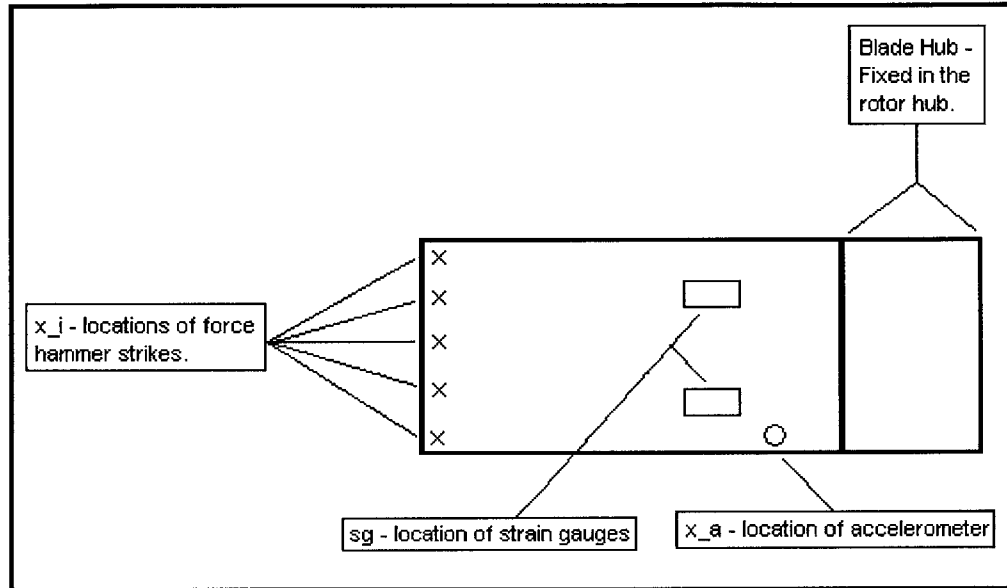
Figure 3.2: Blade Layout for Force Hammer Testing

Then, the blade was struck at five different locations along the tip, producing a frequency response function for each location. Each of the locations where the blade was struck by the force hammer is shown in Figure 3.2, labeled x_i. These locations are very close to the full span of the blade, and are spaced at 0.5-inch intervals.

While this method is less intuitive, it yields equivalent information about the behavior of the blade by using the "Reciprocity Theorem." If we define the following functions:

- A(x_a) – Accelerometer response at position of the accelerometer, x_a. This can be measured;

- F(x_i) – Input force from force hammer at the ith position along the blade tip, x_i. This can also be measured, and a frequency response function between this input and A(x_a) was obtained as described above;

- A(x_i) – Accelerometer response at ith position along the blade tip, x_i, if the accelerometer caused negligible blade loading. This cannot actually be measured;

- F(x_a) – Input force from force hammer at position of the accelerometer. This force is not measured.

The Reciprocity Theorem states: "If a force generator operating at a particular frequency at some point (1) in a system of linear bilateral elements produces a velocity at another point (2), the generator can be removed from (1) and placed at (2); then the former velocity at (2) will exist at (1), provided the impedances at all points in the system are unchanged."[9] This theorem comes from the mechanical analog of an electric circuit. Essentially, a mechanical structure can be treated as a system of springs, masses, and dampers. Any mechanical system of this form has an electrical circuit analogy. The reciprocity theorem was originally derived for electric circuits, and then extended to mechanical systems. The requirement for "linear bilateral elements" is satisfied by a continuous material, according to (2). Thus, using the reciprocity theorem, it can be stated that:

$$\frac{A(x\_a)}{F(x\_i)} = \frac{A(x\_i)}{F(x\_a)} \qquad \text{Equation 3.1}$$

A(x_a)/F(x_i) is the frequency response function that can be measured directly, using the force hammer and the accelerometer. However, what is desired is A(x_i)/F(x_a), which relates the force hammer input to the blade response at the tip. Thus, using the reciprocity relation, the desired function is simply equal to the measured function.

These transfer functions were determined for each of the five locations, x_i, along the blade tip, for both the bending and torsion blade. The blade was struck with the force hammer at each x_i approximately 40 times, and the signal analyzer averaged the response information from all of the strikes to produce a frequency response function for each location. A representative frequency response function is shown in Figure 3.1. Finally, using the "Matlab" function "invfreqs" a least square fit to the data was created, which eliminates some of the noise in the data. This fitted function will be referred to as H-hat. An example of fitting H-hat to the data is shown in Figure 3.3. The raw data is shown in blue, while H-hat is shown in red. H-hat appears to fit accurately the raw data in the frequency range near the two modes.

37
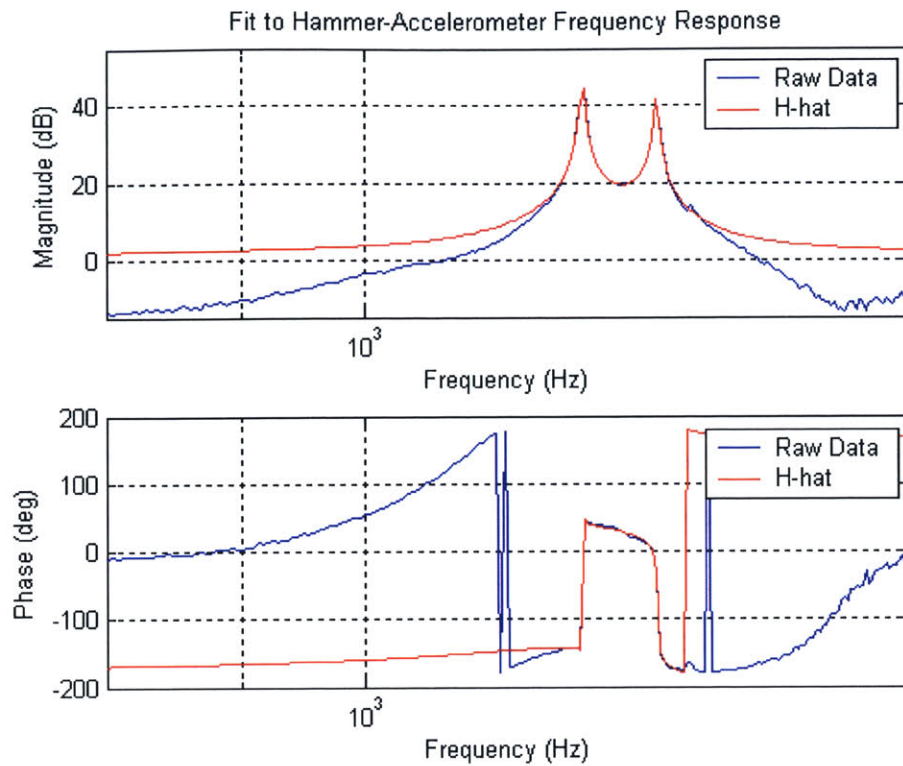
Figure 3.3: Example of H-hat fit to Frequency Response Function

The frequency response functions between the hammer and accelerometer were used to estimate the mode shapes at the two resonant frequencies identified in Table 3.1 for each blade. For each of these two resonant frequencies, five data points of H-hat around these frequencies (the value at the resonant frequency, and at the two closest frequencies that were higher and lower than the resonant frequency) were selected for each of the five blade locations. Each of these ranges of H-hat have magnitude and phase values, as shown in Figure 3.4 and Figure 3.5 for the 1208 Hz mode for the bending blade.
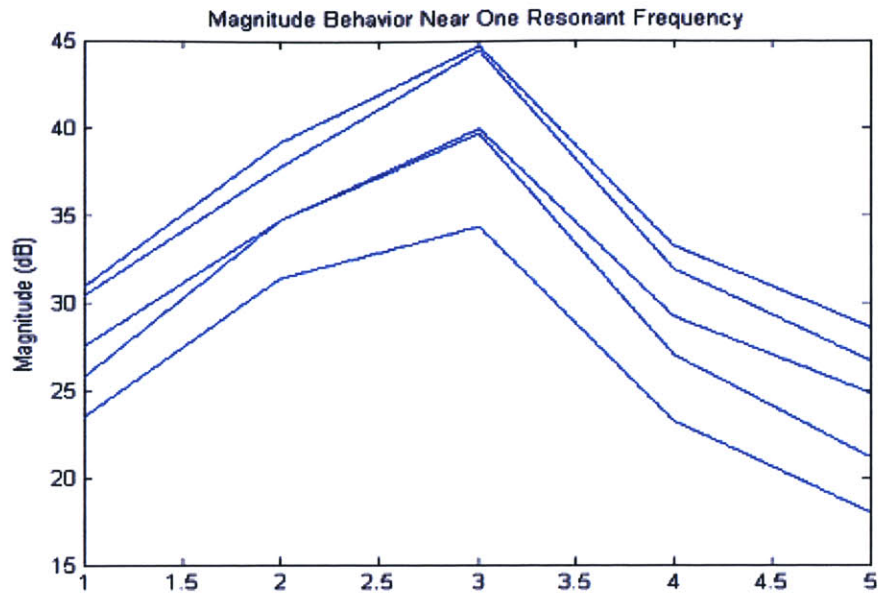
Figure 3.4 – H-hat Magnitude near 1208 Hz Mode
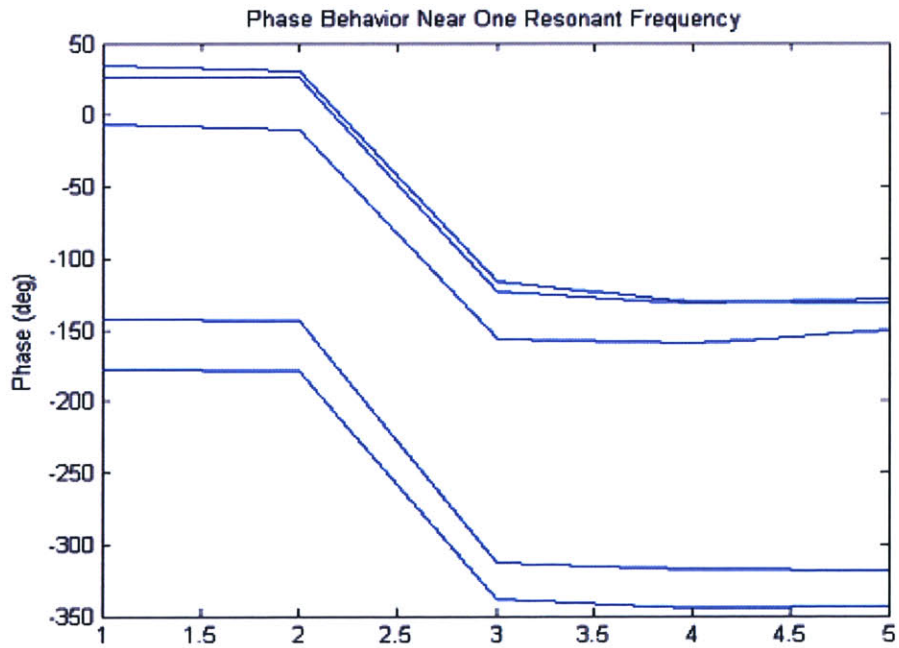
Figure 3.5 - H-hat Phase near 1208 Hz Mode

These figures show the behavior of the magnitude and phase for each of the blade locations, x_i, in the frequency range around the 1208 Hz mode for the bending blade.

The third point in each of the figures corresponds to the data point at 1208 Hz. At each position x_i the blade vibrates sinusoidally with a magnitude (M) and a phase (φ):

$$A(x\_i) = M_i * \cos(\omega * t + \phi)$$ Equation 3.2

For each of the two resonant frequencies for the bending and torsion blade, x_1 was chosen as a baseline, with a relative vibration magnitude of unity, and relative phase of zero. Each of the other locations vibrates with a relative magnitude M_i/M_1, and a relative phase difference Phi_i – Phi_1. The relative magnitude was calculated as the ratio, r_i, that satisfied M_i*r_i=M_1 in a least squares sense, for the range of five points around each resonant frequency. Specifically, the ratio, r_i, is such that it minimizes the error, e, given in Equation 3.3.[10] m_i and m_1 are row vectors with five elements, containing the magnitude of the frequency response function at the five points around the resonant frequency.

$$\|e\|^2 = \|m\_i * r\_i - m\_1\|^2$$ Equation 3.3

Minimization of $\|e\|^2$ is performed using Matlab's "inverse" function, which is applied to the following syntax in Equation 3.4 in order to solve for each r_i.

$$r\_i = \left(m\_i^T * m\_i\right)^{-1} * m\_i^T * m\_1$$ Equation 3.4

where: m_i = row vector of size 1x5

m_i^T = transpose of m_i, column vector of size 5x1

m_1 = row vector of size 1x5

The relative phase difference was just the average of Phi_i – Phi_1 over the same range, for both resonant frequencies and both blades. In this way, the magnitude and phase, relative to the baseline location x_1, was calculated for each of the other four locations, at both resonant frequencies. A time history of the mode shape was then plotted for both frequencies, in which each of the five blade locations vibrates sinusoidally, with a magnitude equal to its relative magnitude, and phase equal to its relative phase difference. The two modes for the torsion blade are shown in Figure 3.6 and Figure 3.7. The bending blade exhibited similar behavior, but at slightly different frequencies, as

40

shown in Table 3.1. The mode at 1176 Hz appears to be a torsion mode, while the mode at 1236 Hz seems to be a bending mode.
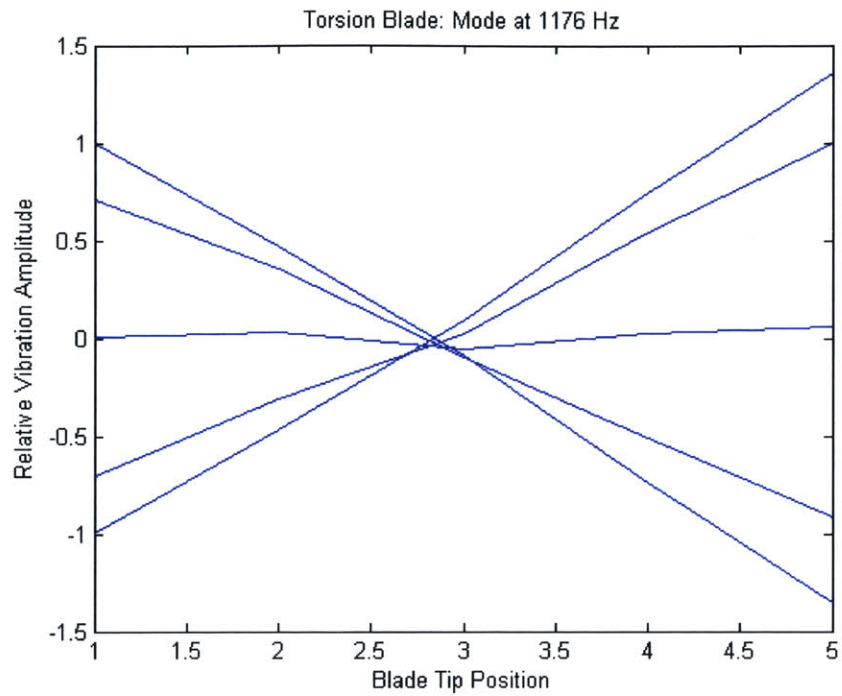
Figure 3.6: Mode Shape at 1176 Hz
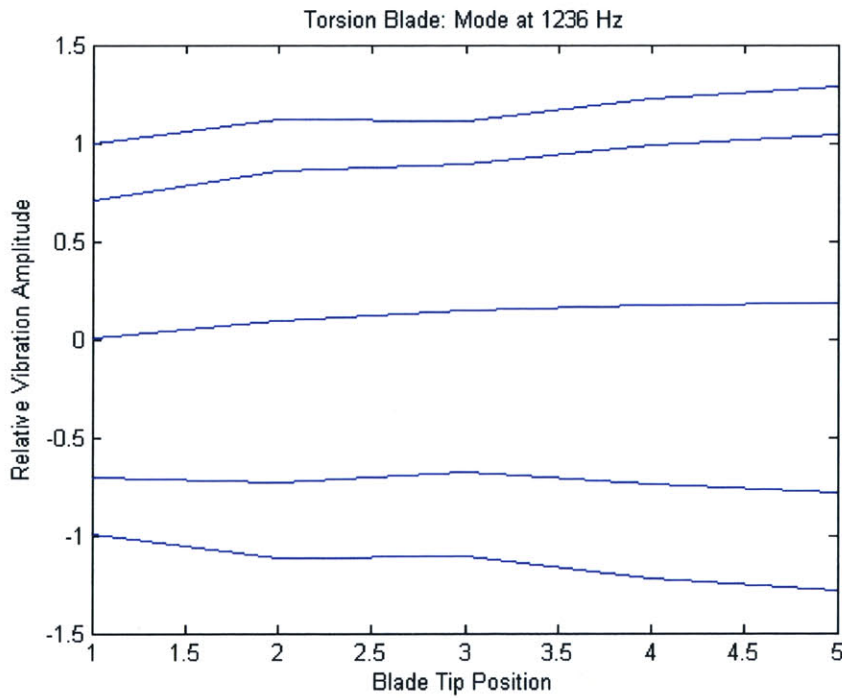
Figure 3.7: Mode Shape at 1236 Hz

3.1.4 Strain Gauge Transfer Functions

Strain measurements are what can actually be measured using the strain gauges. Therefore, another transfer function must be developed which relates the strain gauge readings to the hammer input, for both the bending and torsion blade. The accelerometer was removed from the blades, and the blades were struck with the force hammer at the location where the accelerometer used to be located, x_a (See Figure 3.2). A frequency response function between the force hammer strikes at this location and the strain gauges, located at position sg in Figure 3.2, was created using the signal analyzer. As before, the blade was struck approximately 40 times, and each of the strikes was averaged to produce a frequency response function with low noise. This frequency response function can be designated:

$$\frac{S(sg)}{F(x\_a)}$$

where S(sg) is the strain gauge reading at the location of the strain gauge, sg, and F(x_a) is the input force from the force hammer at location x_a, where the accelerometer used to be located. This was done for the bending blade and the torsion blade. Once again, the "invfreqs" function was used to fit a function to the data. This fit was called G-hat. The last step was to combine the two transfer functions to obtain the desired transfer function:

$$\frac{A(x\_i)}{S(sg)} = \frac{A(x\_i)}{F(x\_a)} / \frac{S(sg)}{F(x\_a)} \qquad \text{Equation 3.5}$$

This final transfer function was obtained by dividing the raw data from each of the five hammer-accelerometer frequency response functions, by the raw data from the hammer-strain gauge frequency response function. This yields the final transfer functions, $A(x\_i)/ S(sg)$, between the strain gauge data and the amplitude of the tip acceleration for each of the five blade tip locations. Again, the "invfreqs" function was used to create a least square fit to the final transfer function. An example of the final transfer function for one blade tip location for the bending blade is shown in Figure 3.8. The large peak occurs at 1208 Hz. This peak appears because the hammer-accelerometer frequency response has a mode at 1208 Hz, but the hammer-strain gauge frequency response has no

such peak because the strain gauges on the bending blade do not sense torsion modes. There is no peak in the final transfer function at 1284 Hz, the bending mode resonant frequency. There is no peak at 1284 Hz because the peak in the hammer-accelerometer frequency response and the peak in the hammer-strain gauge frequency response occur at the same point, and so when these two functions are divided the peak is eliminated.

Fit to Hammer-Accelerometer Frequency Response
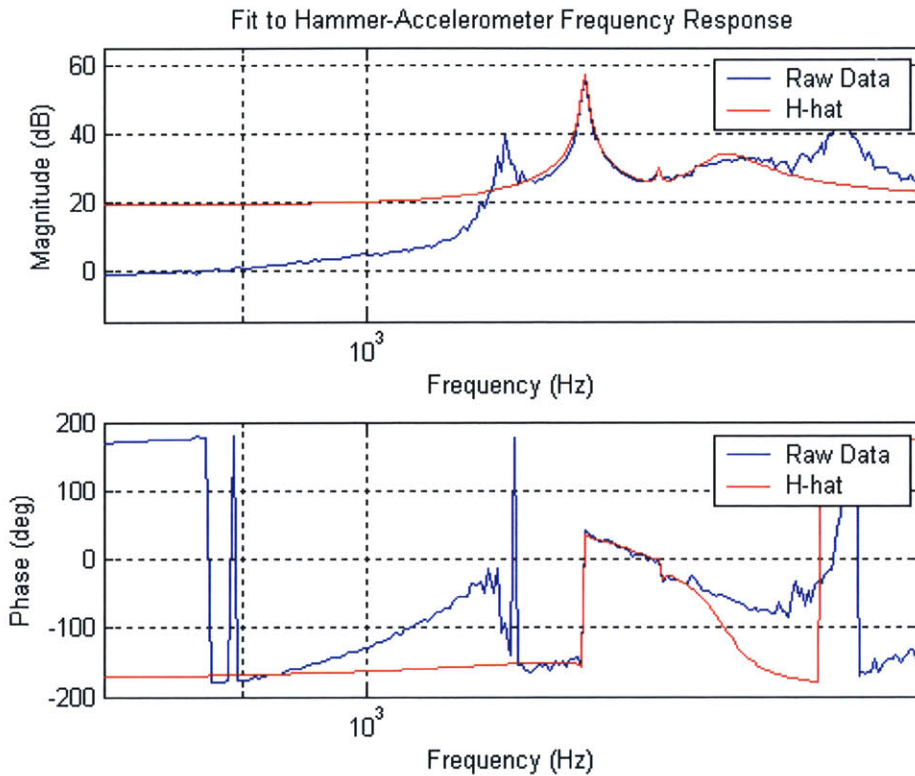
Figure 3.8: Example of Final Transfer Function and Fit

These final transfer functions, one for each blade tip location, can be used to predict the blade tip behavior based on strain gauge measurements. For the bending blade, the values of the transfer functions at 1284 Hz are chosen. These values are just complex numbers. These complex numbers can then be implemented as a digital filter in "Matlab." These filters can be applied to the strain gauge data, yielding estimates of the blade tip behavior at each of the five blade tip locations.

3.2 Finite Element Dynamic Analysis

Finite element analysis (FEA) provides an alternative means of determining the mode shapes and resonant frequencies of a structure, and provides a check on the hammer testing described in Section 3.1. "Pro/Mechanica" is a finite element analysis tool that is linked to Pro/Engineer, a computer aided design (CAD) tool, and was used for the FEA in this thesis.

3.2.1 Finite Element Analysis Background

FEA is a well-known structural analysis tool. Much has been written about the basis of FEA, so only a short summary will be given here. FEA begins by importing a CAD model, which is a model of the structure to be analyzed, created in a CAD program like Pro/Engineer. Next, simulation parameters are applied to the structure. Simulation parameters include material properties, applied loads, and constraints. In the next step, the model is discretized to form a finite element mesh. The model is broken up, or discretized, into small finite elements that collectively approximate the shape of the model.[11] These finite elements are 3-D, tetrahedral or 8-node shapes. These elements together make up the finite element mesh. In Pro/Mechanica, meshing is done automatically. Once the mesh is created, the governing equations of the system are solved. The governing equations are a set of partial differential equations (PDE's). The dependent variable is the displacement, and the solutions are such that the equilibrium position minimizes the total potential energy of the system.[12] For a FEA solution, values of displacement are only calculated at the nodes of each element. The variation of displacement within the element is calculated using the values at the nodes, and approximately solves the governing PDE.[12] The loads, constraints, and shape of the model provide the boundary conditions for solving the PDE. Once the displacement is calculated, the strain in the structure can be calculated by taking the spatial derivative of the displacement. Finally, the stress is calculated by multiplying the strain by the stiffness matrix. In this way, the displacement, stress, and strain of a structure can be calculated. A FEA program can also perform a dynamic analysis of a structure. In a

dynamic analysis, the mode shapes and corresponding resonant frequencies are also calculated.

3.2.2 Dynamic Analysis of Simplified Blade Model

The test blade, discussed in Section 2.2, has a geometry that is too complicated for Pro/Mechanica to analyze. Instead, a simplified rectangular model of the test blade was used in the FEA. A picture of the simplified model appears in Figure 3.9.
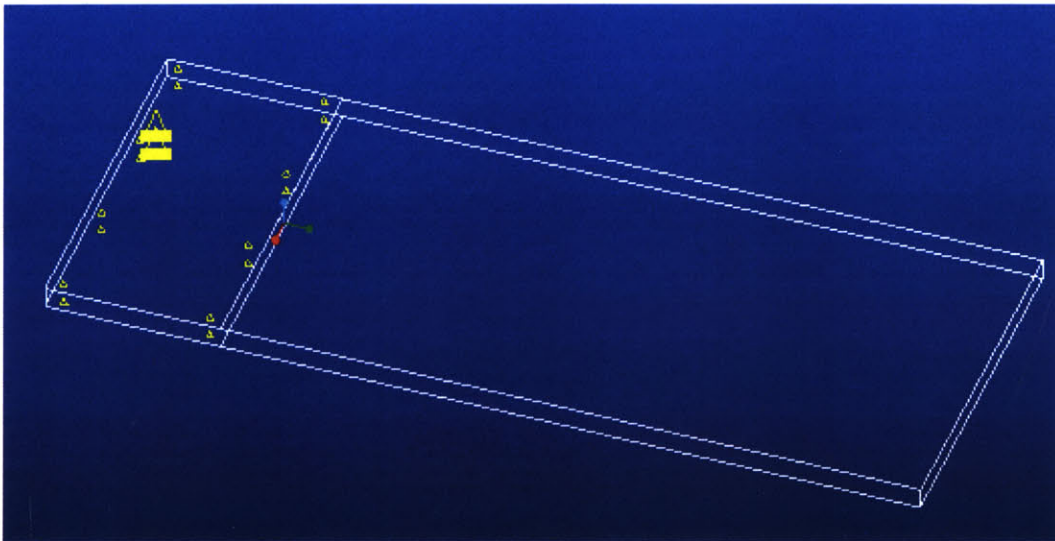
Figure 3.9: Simplified Blade Model

The simplified blade model has the same span and chord as the test blade. The thickness of the simplified model is the approximate average thickness of the test blade, about 0.1 inches. The hub of the test blade was approximated as the 1-inch segment at the root of the blade. In Pro/Mechanica, the surfaces of the hub section were constrained, in order to approximate the actual constraints on the test blade in the spin pit rotor. The constrained surfaces are denoted by the yellow marks in Figure 3.9. The material selected was aluminum 2024, which is what the test blade was fabricated from.

The dynamic analysis calculated the mode shape and the resonant frequencies of the first four modes for the simplified blade model, i.e. the four lowest frequency modes. The

FEA outputs are plots of the displacement, stress, and strain for each of the modes. The displacement results for two of the modes are shown in Figure 3.10
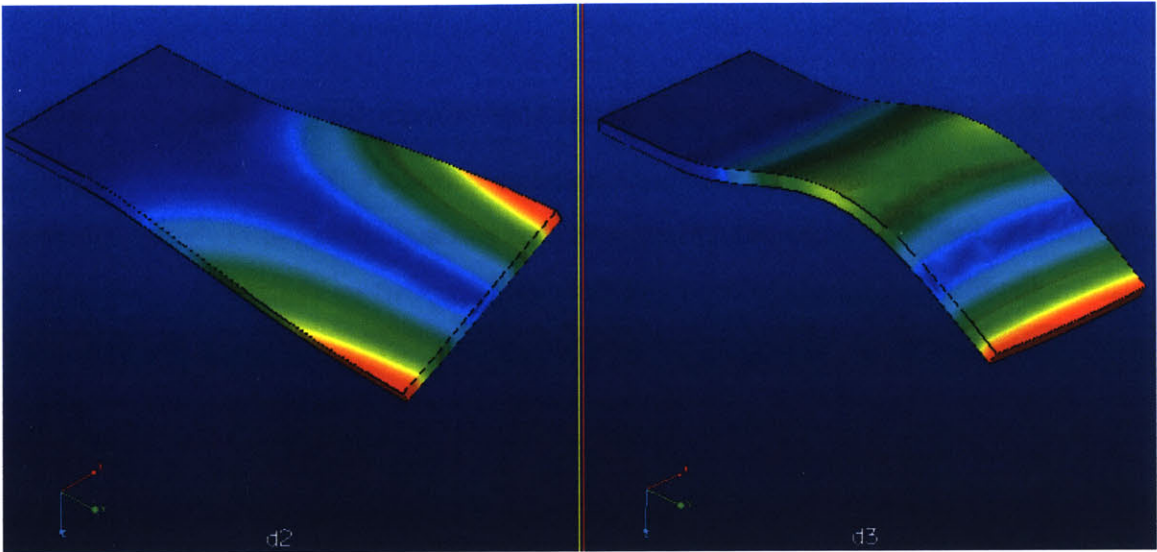
Figure 3.10: Mode Shapes for Second and Third Mode of Simplified Blade

The modes shown in Figure 3.10 are the second and third modes of the simplified blade. The second mode is shown on the left, and appears to be a simple torsion mode. The third mode is shown on the right, and appears to be a second bending mode. The displacement is presented on a color scale, where blue is the minimum displacement, and red is the maximum displacement. The first mode is a simple first bending mode, and is not shown here. The frequencies of these modes are given in Table 3.2.

Mode Type	Torsion – Mode 2	Bending – Mode 3
Frequency	1077 Hz	1601 Hz

Table 3.2: FEA Resonant Frequencies for Simple Blade Model

These two modes serve as a comparison and check of the hammer testing results discussed in Section 3.1. The results of the hammer testing, given in Table 3.1, showed a torsion mode at approximately 1190 Hz, and a bending mode at approximately 1260 Hz. While the FEA results do not exactly match the hammer testing results, they do provide a qualitative confirmation of the results. Both the FEA and the hammer testing show that the second mode is a torsion mode, and the third mode is a bending mode. The resonant frequencies do not exactly match, but they are on the same order, in the range of 1-2 kHz.

These discrepancies are not surprising. The simplified blade model, while having similar dimensions to the test blade, has a much different cross section, thickness distribution, and constraints. These differences are sure to alter the mode shape and frequencies somewhat. The qualitative similarities are the best that could be hoped for. In sum, the FEA confirms the results of the hammer testing, indicating a torsion mode and a bending mode at frequencies near the results of the hammer testing.

3.3 Dynamic Balancing of Spin Pit Rotor

Dynamic unbalance is a common source of vibration in rotating machinery. Dynamic unbalance is characterized by a misalignment between the axis of rotation and the rotating center of mass. That is, while the rotor spins, the center of mass rotates around the axis of rotation. This unbalance of the rotor causes the rotor to vibrate at the same frequency as the rotor rotation frequency. This can lead to extra loading on the rotor bearings, and therefore reduced bearing lifetime. In order to prevent excessive bearing loading, the spin pit rotor must by dynamically balanced. An in-situ balancing scheme was used to balance the rotor and minimize rotor vibrations, and will be described here.

3.3.1 Theoretical Basis for Balancing Scheme

A graphical method can be used to balance the rotor. Dynamic unbalance occurs when the center of mass of a rotor does not lie on the axis of rotation. The magnitude of the unbalance will be called U. U can be measured in several ways; for the purposes of this thesis, U will be the amplitude of the vibration of the unbalanced rotor. U can be measured with an accelerometer placed on the bearing housing. While the center of mass rotates around the axis of rotation in the stationary frame, in the rotating frame, U always points in one direction. Thus, in the rotating frame, U can be treated as a vector, with magnitude U, and unknown orientation. The point of the balancing procedure is to determine the magnitude and direction of U. If this is known, then positioning some mass in the opposite direction of U can offset the unbalance. This is the basis of the balancing scheme. First, a simplified version of the balancing scheme will be described

in order to elucidate the underlying geometric basis. Then, a more complicated version will be described, which represents the actual scheme used in the spin pit.

The magnitude of U can be determined easily by running the rotor at a desired speed, and then measuring the amplitude of the unbalance using an accelerometer. This will not yield the orientation of U however. In order to determine the orientation of U, a system of trial weights can be used. A weight of known mass, m_t, is placed at two different locations on the rotor, 90° apart from each other, and at the same radius. Each time the trial mass is positioned at one of these two locations, the rotor is run, and the vibration amplitude is measured. The magnitude of each of these vibration measurements is denoted R1 and R2. This situation is shown graphically in Figure 3.11.
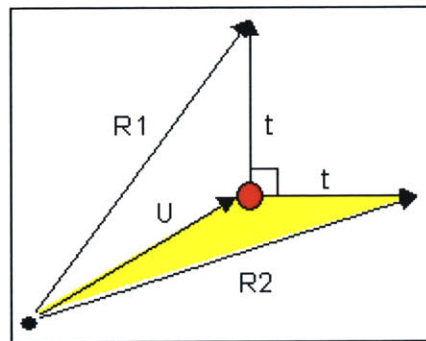
Figure 3.11: Simplified Balancing Setup Geometry

The axis of rotation is the black circle. The vector U is shown in an unknown direction. The vector t is the magnitude of the unbalance due only to the trial mass. There are two t vectors because the trial mass has been placed at two locations, which are each separated by 90°. However, t cannot be measured. R1 and R2 are also shown in Figure 3.11. Each of these vectors is the vector sum of U and t, depending on the position of the trial mass. For example, the magnitude of the unbalance measured when the trial mass is located at position 1, is equal to the vector sum of the unbalance with no trial mass, and the unbalance of just the trial mass located at Hub 1. This measurement is therefore R1. Thus, the geometric situation shown in Figure 3.14, indicates the effect of the trial mass on the original unbalance of the rotor.

The orientation of U and the magnitude of t can be solved for by geometrically manipulating Figure 3.11. First, the yellow triangle in Figure 3.11 is rotated 90° counterclockwise to produce the situation shown in Figure 3.12.
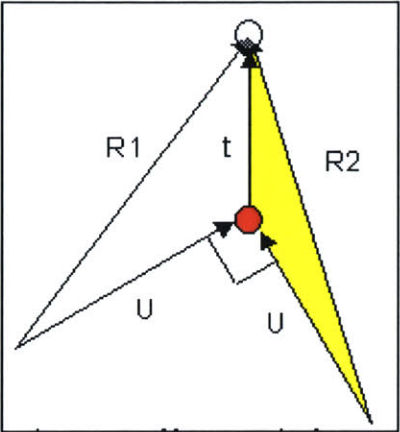
Figure 3.12: Manipulated Geometry

Next, a circle can be drawn, centered at the red dot, of radius U. This circle will then intersect both of the U vectors in Figure 3.12. Finally, at the points where the U vectors intersect the circle, two more circles are drawn, one of radius R1, and one of Radius R2. The result is shown in Figure 3.13. The blue and green circles are of radius R1 and R2, respectively. These circles intersect each other at two points, one of which is a distance t away from the center of the red circle. In this way, the magnitude of t can be determined. Once the magnitude of t is determined, the orientation of U can be determined easily using Figure 3.11.
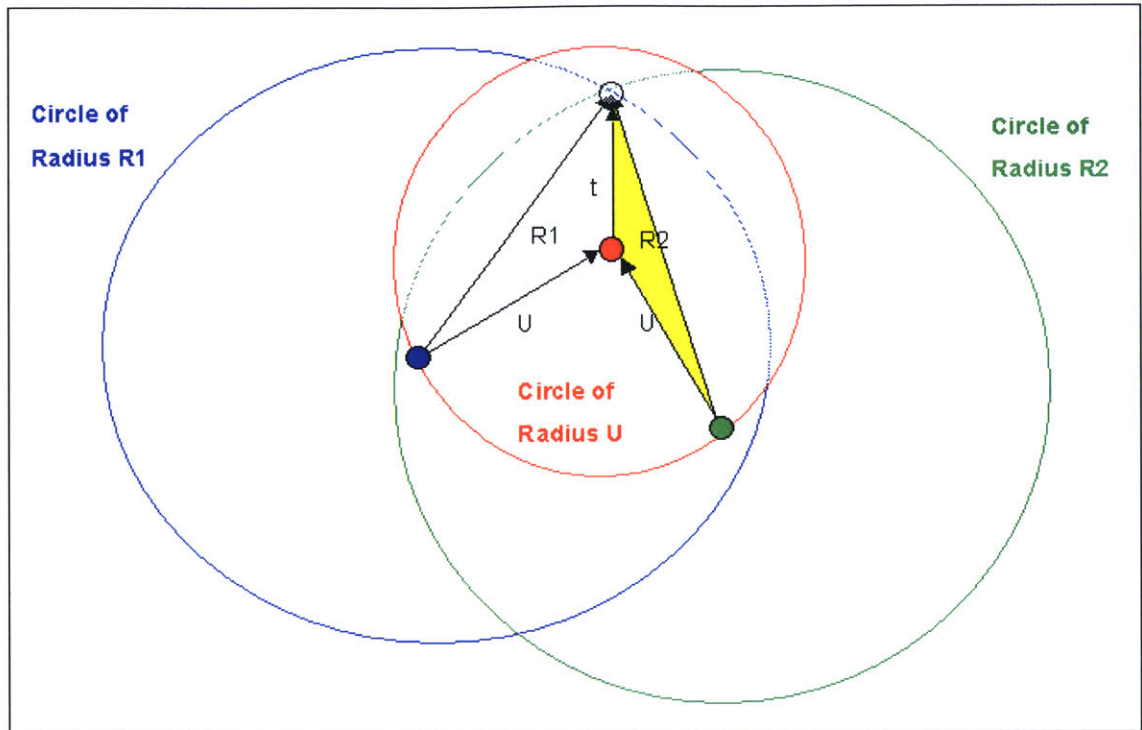
Figure 3.13: Manipulated Geometry with Circles

The situation in the spin pit is more complicated because the trial mass can only be positioned on the struts, which are each 120° from each other. Nonetheless, the geometric formulation can be extended to this situation as well. Once again, the magnitude of U is measured first. Then, the magnitude of R1, R2, and R3 are measured by placing the trial mass at each of the three hub positions. The resulting geometry is shown in Figure 3.14. Again, R1, R2, and R3 are the vector sums of U and t, depending on the location of the trial mass.
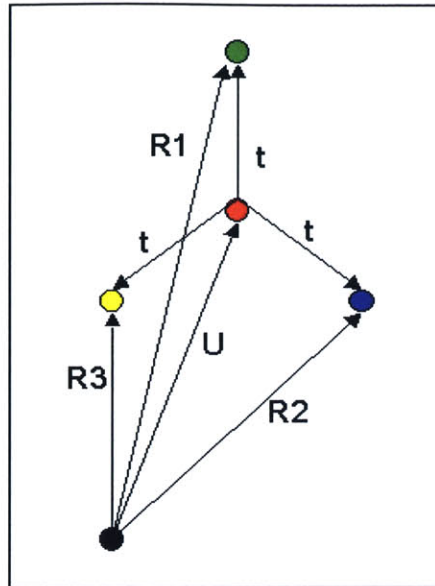
Figure 3.14: Geometry of Unbalance

The solution to find the magnitude of t and the orientation of U proceeds as follows, and is analogous to the simpler situation described above using two trial mass locations. A circle of radius U is drawn about the axis of rotation, the black dot in Figure 3.14. At the position on this circle where the hubs would lie, circles of radius R1, R2, and R3 are drawn. The intersection point of these three circles is a distance t from the center of circle of radius U, and is in the direction opposite U. The vector from the origin to this point is denoted B. Thus, by simply finding the intersection of these circles, the magnitude of t and the orientation of U are determined. These results appear in Figure 3.15.
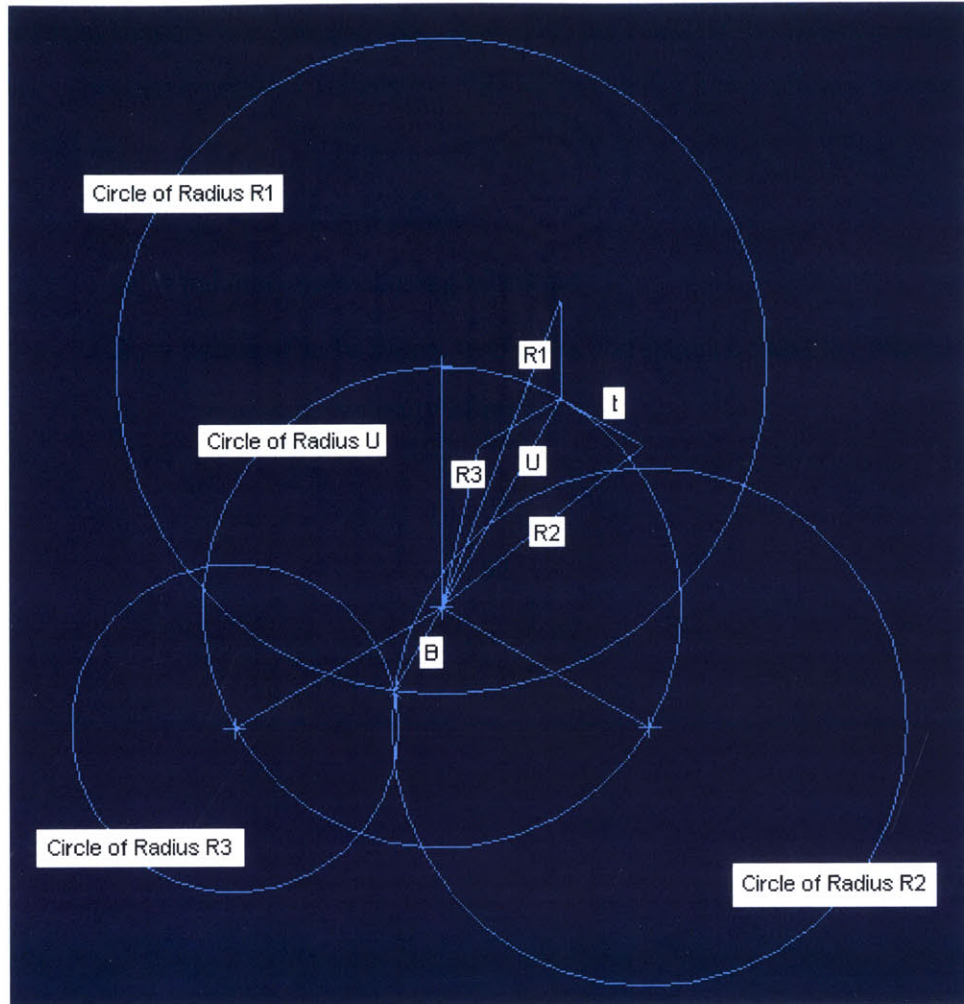
Figure 3.15: Balancing Solution

Next, a balancing mass must be positioned on the rotor to counteract the unbalance U. The position of the balance mass is known – it is in the direction of B, at the same radius where the trial masses were positioned. However, the mass of the balance mass is as yet unknown. This can be solved for easily. The force causing rotor vibrations due to U can be expressed as:

$$|U| \propto m_u R_t \omega^2 \qquad \text{Equation 3.6}$$

where: m_u = balance mass causing vibration U

R_t = radius of hubs where trial mass and balance mass are placed

ω = angular velocity of rotor

The force generated by the trial mass can be expressed as:

$$|t| \propto m_t R_t \omega^2$$ Equation 3.7

where: m_t = trial mass

Thus, the magnitude of both U and t are proportional to the mass causing the unbalance, m_u and m_t, respectively. Solving for m_u yields:

$$m_u = m_t \frac{|U|}{|t|}$$ Equation 3.8

The trial mass is known a priori. The magnitude of U is measured in the initial run, and the magnitude of t is found using Figure 3.15. Thus, it is possible to solve for m_u. To eliminate the unbalance, a weight of mass m_u is placed at the radius of the trial mass, in the direction of the vector B from Figure 3.15. This balance mass will produce an unbalance vector of magnitude U, in the opposite direction of U. The net effect is to remove the unbalance of the rotor, so that the center of mass and the axis of rotation are in line.

3.3.2 Balancing Equipment

The procedure for dynamically balancing the spin pit rotor has been described in Section 3.3.1. The actual measurements for the magnitude of the unbalance are made using an accelerometer, located at the housing of a bearing. A B&K charge condition amplifier then amplifies the signal from the accelerometer. The output of the amplifier can then be seen on an oscilloscope, where the amplitude of the vibration can be measured. The trial mass used in the balancing procedure is just a small bolt with a few nuts attached. The bolt can be screwed into holes that have been drilled into the struts.

In sum, the rotor balancing scheme described here can dynamically balance the rotor using a total of five runs. The only equipment needed is an accelerometer, amplifier, and oscilloscope. This scheme provides a quick means of balancing, and the rotor can be

rebalanced at any time, in case different blades are used. One caveat to the balancing procedure is the effect of rotor speed. As shown in Equation 3.6, the unbalance is proportional to the square of the rotor speed. At high speeds, the unbalance can generate a substantial force on the rotor bearings. If the rotor is balanced at a low speed, it should probably be rebalanced when it is run at a higher speed.

3.4 Verification of Test Blade Excitation

This thesis aims to detect blade vibrations using an ECS. Therefore, the blades must be vibrating as they rotate in the spin pit rig. In Section 2.5, three arrays of magnets were described which were used to excite the blades. The magnets impart a force on the blades, and the frequency of this excitation is proportional to the rotation speed of the blades. The relationship between excitation frequency and rotation frequency is given in Equation 2.4, which is given again below.

$$F_{EX} = F_{ROT} * \frac{2\pi}{\Delta\theta}$$
<div align="right">Equation 2.4</div>

In order to ensure that the magnets excite the modes of the blades, a test run was performed. The verification was performed using the bending blade, described in Section 2.4. The strain gauges on the bending blade were positioned to detect bending modes. The resonant frequency of the bending mode for this blade was found to be 1284 Hz (Table 3.1) using the hammer testing described in Section 3.1. In order to excite a mode at 1284 Hz, the rotor should be spun at approximately 18.5 Hz according to Equation 2.4. Blade vibrations were verified in two ways. First, as the rotor was spinning, the strain gauge output was connected to the digital signal analyzer. The signal analyzer calculated a power spectral density (PSD) of the strain gauge output. The PSD was plotted as a function of frequency. The rotor speed was then adjusted until a prominent peak appeared at 1284 Hz on the signal analyzer. When the peak occurred, it indicated that the strain gauge output was oscillating at a frequency of 1284 Hz, and so it can be inferred that the blade is vibrating at this frequency, which is its resonant frequency. An example of a PSD on the signal analyzer is shown in Figure 3.16.
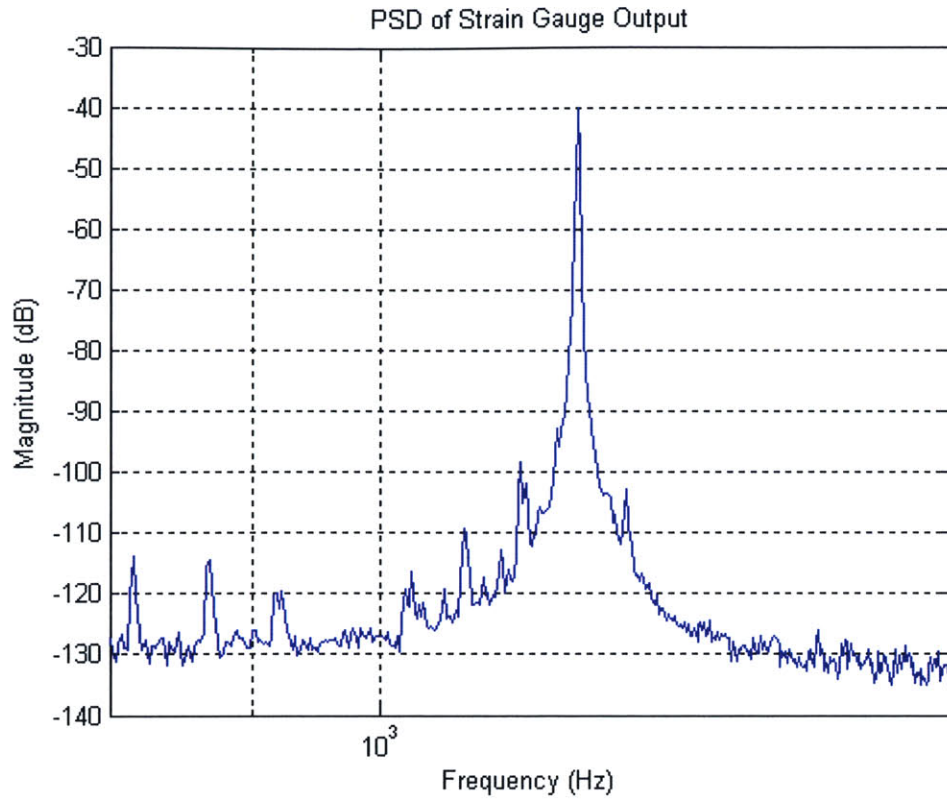
Figure 3.16: Example of PSD of Strain Gauge Output for Torsion Blade

Once the signal analyzer indicated that the blade was vibrating at 1284 Hz, strain gauge data was taken using the A/D board. This data was then loaded into Matlab. The strain gauge output displayed a good deal of noise in Matlab, and blade vibrations were difficult to identify. A segment of the strain gauge output appears in Figure 3.17.
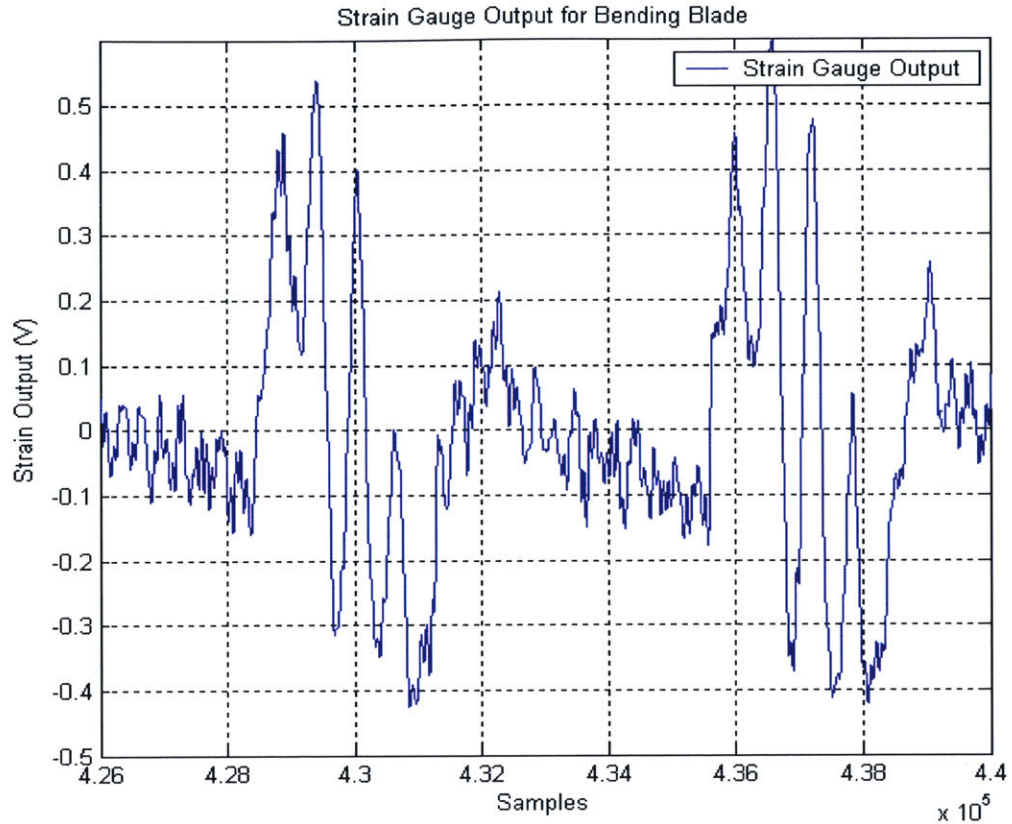
Figure 3.17: Strain Gauge Output

The two regions of very high amplitude output are not vibrations. Rather, those regions occur every time the blade passes the magnet arrays. Apparently the magnetic field of the magnets produces a signal in the strain gauges. This electromagnetic pickup was ignored. The blade passes a magnet array every 1/3 of a revolution, so each segment of data between the regions of pickup represent just under 1/3 of a revolution of strain gauge output. In Figure 3.17, the output between the regions of pickup shows some periodic behavior. However, it appears inconsistent and noisy. In order to eliminate noise and rotation-to-rotation variations, the strain gauge output was averaged over each revolution. This "ensemble average" was performed in Matlab. The strain gauge data was broken up into 1-revolution segments. These segments are approximately 21,600 samples long, which is just the sampling frequency divided by the rotation speed, as shown in Equation 3.9. These segments were determined using a reference point from the ECS signal. The details of this process are described in Section 4.2.2.

56

$$1\_\mathrm{Re}\,volution = \frac{400{,}000\left(\dfrac{Samples}{Sec}\right)}{18.5\left(\dfrac{\mathrm{Re}\,v}{Sec}\right)} = 21{,}600\left(\frac{Samples}{\mathrm{Re}\,v}\right) \qquad \text{Equation 3.9}$$

Each of these time samples were summed and then divided by the total number of revolutions to produce an ensemble average of the strain gauge data. The ensemble average is shown in Figure 3.18.
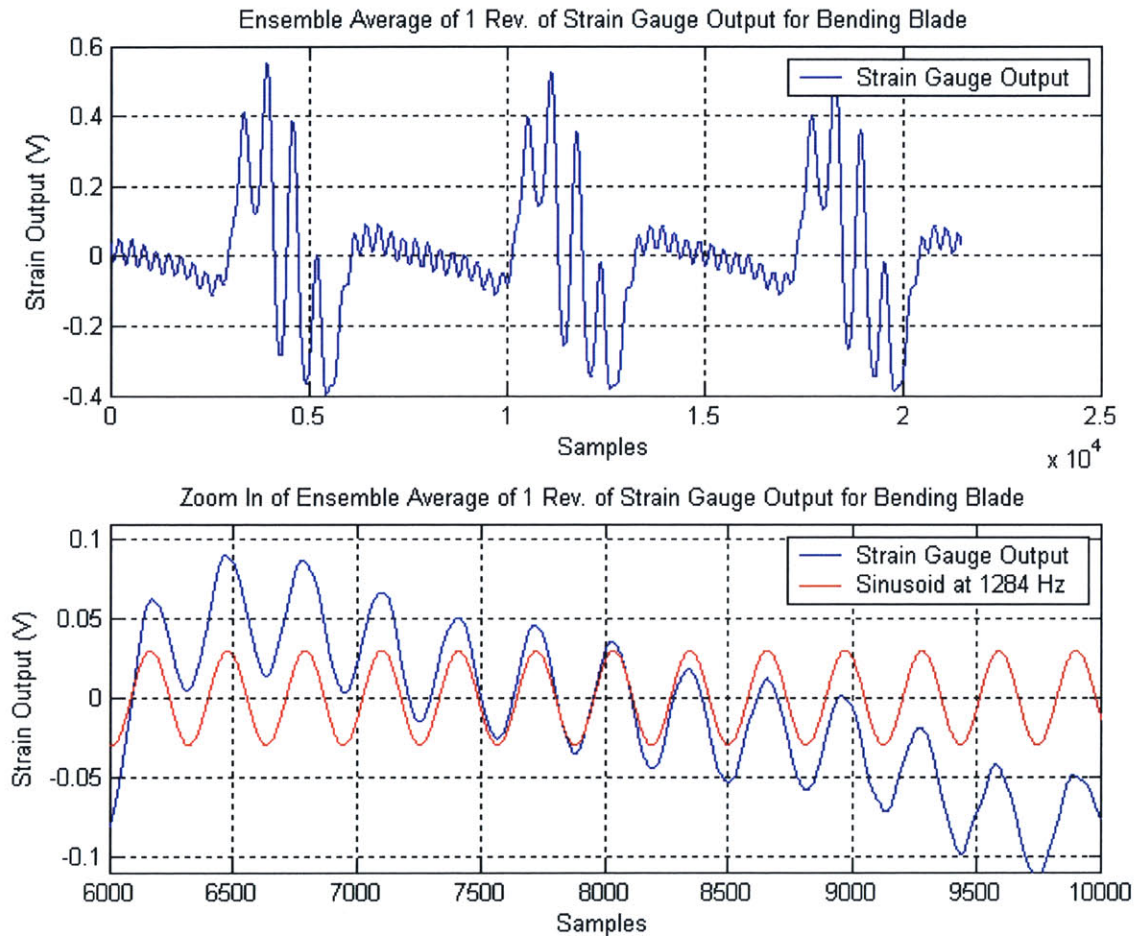
Figure 3.18: Ensemble Average Results

The top plot is the entire ensemble average, while the bottom plot zooms in on a segment of the ensemble average between two of the regions of pickup. The top plot shows a much cleaner signal than the data in Figure 3.17. The ensemble average removes much of the noise and variations seen in the raw data. On the bottom plot, a red sinusoid is also plotted. This sinusoid has a frequency of 1284 Hz. It was plotted in order to ensure that

the vibration seen in the ensemble average is at the expected frequency. This plot shows clearly that the sinusoid and the ensemble average have the same frequency. This indicates that the blade is in fact vibrating at 1284 Hz, which is the frequency of the mode that was meant to be excited. The magnitude of the blade tip displacement for both blades will be estimated in Section 4.1.

These results are encouraging. Using Equation 2.4, a rotation speed can be calculated that will cause the magnets to excite the blade at a desired frequency. In this case, the excitation frequency was chosen to be the frequency of the bending mode for the bending blade. The strain gauge output, when viewed on the signal analyzer, shows a prominent peak in the PSD at 1284 Hz. Moreover, when the strain gauge output is ensemble averaged, a clear vibration at 1284 Hz emerges. In sum, this test has verified that the magnets provide an excitation sufficient to excite the desired modes of the blades.

3.5 Eddy Current Sensor Data Output

As the spin pit rotor spins, the test blades will pass the ECS, producing a signature similar to that shown in Figure 1.4. In order to sense blade vibrations using the ECS signature, there should be a minimum of noise in the signal. As mentioned in Section 2.3, a differential amplifier was used for common mode noise rejection. The spin pit rotor produces electro-magnetic noise, which can be picked up by the ECS electronics. The differential amplifier serves to reduce this pickup. A schematic of the differential amplifier that was used is shown in Figure 2.4. The effectiveness of the differential amplifier can be seen in Figure 3.19. The top plot shows ECS data before the differential amplifier was used; the bottom plot shows the ECS data using the differential amplifier. The x-axes for the two plots are on different scales because a different sampling frequency was used for each of the data samples. Also, the orientation of the ECS signal is different for the two plots; this is due to how the differential amplifier was wired.
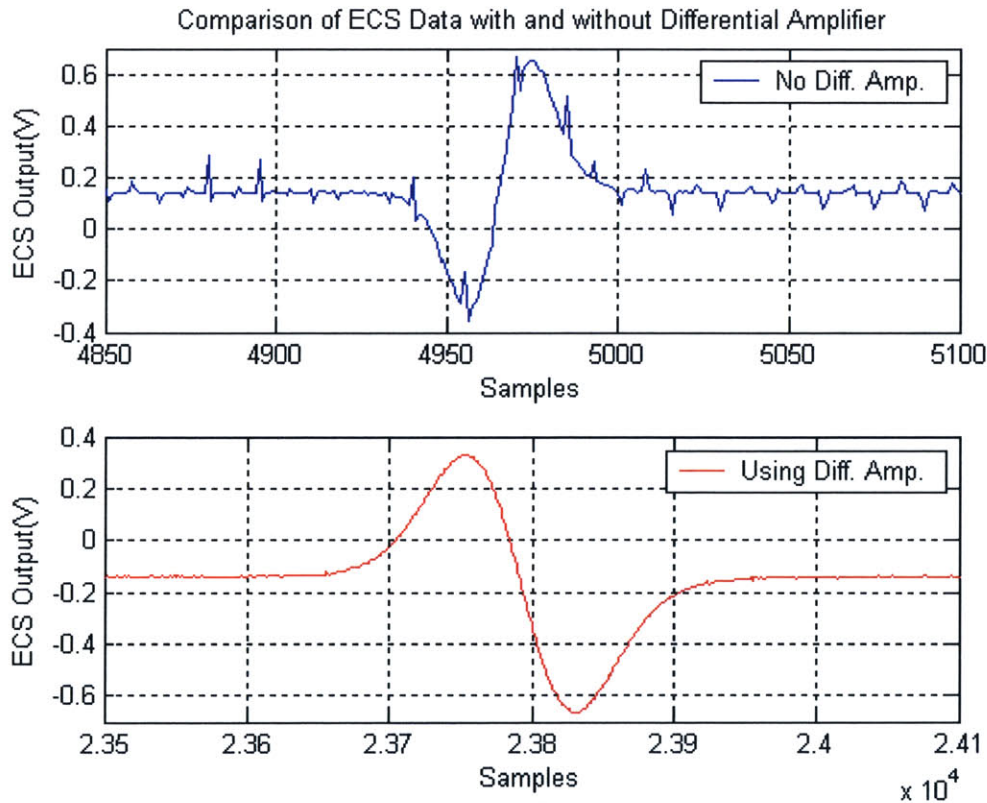
Figure 3.19: Effectiveness of Differential Amplifier

Nonetheless, the comparison demonstrates the utility of the differential amplifier. The ECS signal shown in the top plot has significantly more noise than the signal shown in the bottom plot. By minimizing this noise, a more accurate representation of the ECS signal can be extracted from the spin pit during testing.

To further reduce noise in the ECS signal, a low pass digital filter was employed in Matlab. The filter type was a low pass "fir1" filter. The motor noise has a frequency of approximately 7000 Hz. Therefore, the filter has cutoff band frequencies of 5000 and 7000 Hz, so that signals in the data with frequencies over 7000 Hz are filtered out, but signals in the data with frequencies less than 5000 Hz are unfiltered. The effectiveness of the low pass filter can be seen in Figure 3.20. The data in blue is unfiltered, and the data in red has been filtered. The filtered data is shifted to the right so that the comparison is easier to see.
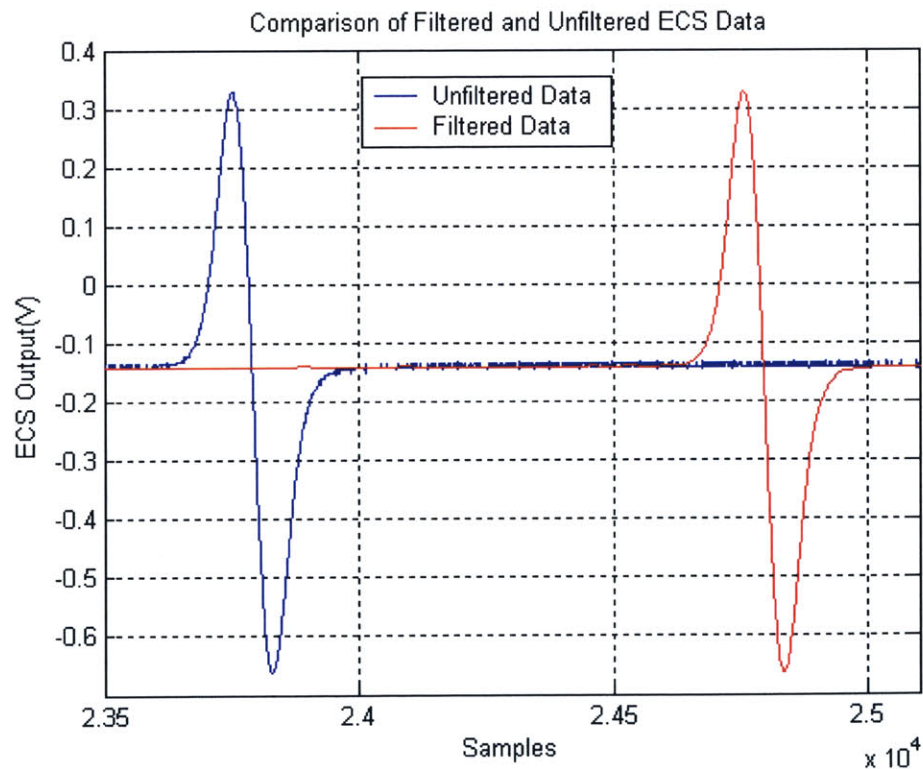
Figure 3.20: Example of Low Pass Filtering

The filter effectively reduces the residual noise in the ECS signal. The steady-state signal between the pulses is especially cleaned-up by the filtering. Thus using both a

differential amplifier and a low pass filter, a clean ECS signal can be extracted from the spin pit with a minimum of noise. A final example of an ECS signal is shown in Figure 3.21.
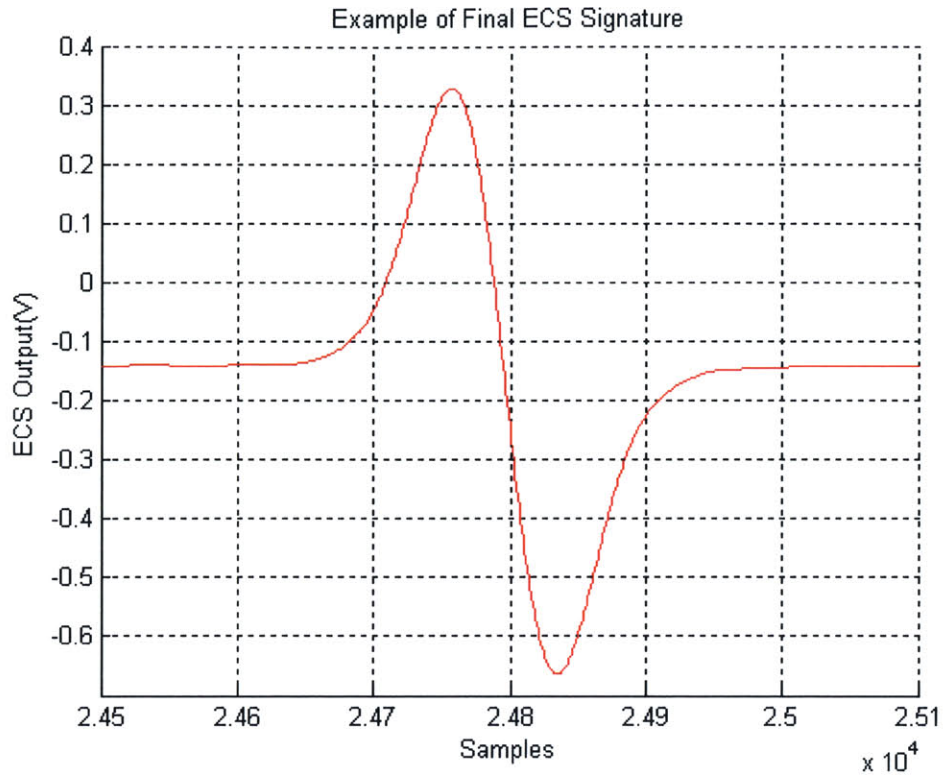
Figure 3.21: ECS Signature with Low Noise

It will be ECS signatures with low noise like that shown in Figure 3.21 that will be analyzed for evidence of vibrations in Chapter 4.

4 Analysis

4.1 Estimate of Blade Tip Displacement

In order to use the ECS to sense blade vibrations, the blade itself must be vibrating. The analysis in Section 3.4 confirmed that the magnet arrays do produce consistent vibrations in the test blades. Beyond knowing that the blade is vibrating, it is also useful to know how much the blade is vibrating i.e. the amplitude of the blade vibration. Combining the force hammer testing from Section 3.1 with the strain gauge data results shown in Section 3.4 provides a means of estimating the displacement of the blade tip due to the vibrations, for both the bending and torsion blade.

The results of the hammer testing were five transfer functions between the strain gauges and the blade tip acceleration. These were denoted as $A(x\_i)/\ S(sg)$, where x_i represents one of the five tip locations. These five transfer function were created for both the bending and torsion blades. As the blade is spinning, strain gauge data can be extracted, which allows for an independent measurement of the strain gauge behavior. The strain gauge data can be ensemble averaged to produce a clear picture of the blade vibrations. An example is shown in Figure 3.18. The amplitude of the strain gauge signal differs between the bending and torsion blade. The torsion blade has an amplitude of approximately 0.04 V, while the bending blade has an amplitude of approximately 0.02 V. These values are also given in Table 4.1.

	Bending Blade	Torsion Blade
Amplitude of Strain Gauge Signal	.02 V	.04 V
Magnitude of Transfer Function	20.0	4.0

Table 4.1: Amplitude of Strain Gauge Signal and Transfer Functions for Both Blades

The magnitude of the tip acceleration can be calculated using the transfer functions calculated in Section 3.1. The magnitude of the tip acceleration is simply the product of the magnitude of the strain gauge signal and the magnitude of the transfer function at the frequency of the mode. The magnitude of the transfer function at the frequency of the

mode can found easily by just taking the absolute value of the transfer function at the point that corresponds to the frequency of the mode of interest. This is shown in Equation 4.1.

$$\|A\| = \|TF\| * \|SG\|$$ Equation 4.1

where: $\|A\|$ = amplitude of the tip acceleration at the frequency of the mode

$\|TF\|$ = amplitude of the transfer function at the frequency of the mode

$\|SG\|$ = amplitude of the strain gauge signal at the frequency of the mode

The frequency of the mode of interest is 1284 Hz for the bending blade and 1176 Hz for the torsion blade, as stated in Table 3.1. The amplitude of the transfer function was taken as the average of the five transfer functions for the bending blade at 1284 Hz. This is because a bending mode should have a nearly constant tip amplitude at all chordwise locations. For the torsion blade, the amplitude of the transfer function was taken as the average of the transfer functions for the two blade tip positions closest to the leading and trailing edge. The amplitudes of the transfer functions for both blades are also given in Table 4.1. Thus, the amplitude of the tip acceleration in Volts can be calculated using Equation 4.1. The results are given in Table 4.2.

	Bending Blade	Torsion Blade
Amplitude of Blade Tip Acceleration	0.40 V	.16 V

Table 4.2: Amplitude of Blade Tip Acceleration for Both Blades

The accelerometer has a conversion factor of:

$$CF = 3.69 \frac{mV}{g}$$

Thus, the blade tip acceleration can be converted to g's using the conversion factor, and then from g's to SI units of m/s^2. These results are shown in Table 4.3.

	Bending Blade	Torsion Blade
Amplitude of Blade Tip Acceleration	1060 m/s^2	430 m/s^2

Table 4.3: Amplitude of Blade Tip Acceleration for Both Blades

Finally, the amplitude blade tip acceleration can be related to the amplitude of the blade tip displacement. If the displacement and acceleration are both assumed to oscillate sinusoidally, then the acceleration is merely the second derivative of the displacement, with respect to time. Therefore, the amplitude of the displacement is related to the amplitude of the acceleration using Equation 4.2.

$$\|D\| = \frac{\|A\|}{\Omega^2}$$
Equation 4.2

where: $\|D\|$ = amplitude of the tip displacement at the frequency of the mode

Ω = frequency of the mode

Thus, the tip displacement amplitude can be calculated using Equation 4.2 and the results of Table 4.3. These results are shown in Table 4.4.

	Bending Blade	Torsion Blade
Amplitude of Blade Tip Displacement	0.64 mm	0.31 mm

Table 4.4: Amplitude of Blade Tip Displacement for Both Blades

In conclusion, the amplitude of the blade tip displacement is approximately 0.3 mm for the torsion blade, and 0.6 mm for the bending blade. These values correspond to the actual displacement of the blade tip while the blades are spinning in the rig and are being excited by the magnet arrays. This calculation was based on the ensemble averaging of the strain gauge signal, from Section 3.4, and the transfer functions determined in Section 3.1.

4.2 Eddy Current Sensor Data

One goal of this research is to detect blade vibrations using an ECS. The blades are made to vibrate using magnet arrays, and the analysis discussed in Section 3.4 demonstrates their effectiveness. As the blades spin in the rig, they will pass the ECS's mounted around the circumference. Each blade passage produces a voltage signal from an ECS. An example of the ECS waveform is shown in Figure 3.21. This section will discuss the analysis that was performed in order to detect blade vibrations in the ECS signal.

4.2.1 Summary of Data Collected

Many data sets have been compiled for this thesis. Each data set consists of two runs in the spin pit. One run has the magnet array installed in the rig, and the other does not. Therefore, the blade is vibrating for one run and it is not vibrating for the other. In this way, the runs can be compared for a data set to see if the presence of blade vibrations affects the ECS signal. The data sets include both bending and torsion data. For some data sets, the rig was run at the speed necessary to excite the bending mode of the bending blade, which is at 1284 Hz. This corresponds to a rotor speed of approximately 18.5 Hz, according to Equation 2.4. For the other data sets, the rig was run at the speed necessary to excite the torsion mode of the torsion blade, which is at 1176 Hz. This corresponds to a rotor speed of approximately 17.0 Hz. During each run, ECS data was taken with one or two of the sensors, and strain gauge data was often taken. A summary of the data appears in Table 4.5.

Data Summary Table

Date	Length of Run (s)	Speed (Hz)	Blade Excited	Eddy Current Sensor	Strain Gauge Data
6/3	5	18.5	Bending	Position 1	Yes
6/9	5	18.5	Bending	Position 1	Yes
6/9	5	18.5	Bending	Position 1	Yes
6/15	5	18.5	Bending	Position 1	Yes
6/16	5	18.5	Bending	Position 1	No
6/21	5	17.0	Torsion	Position 1	Yes
6/22	5	18.5	Bending	Position 1	No
6/22	5	17.0	Torsion	Position 1	No
6/24	5	18.5	Bending	Position 2	Yes
6/24	5	17.0	Torsion	Position 2	Yes
7/12	5	18.5	Bending	Position 1	No
7/12	5	17.0	Torsion	Position 1	No
7/14	10	18.5	Bending	Position 1	Yes
7/14	10	17.0	Torsion	Position 1	Yes
7/23	5	18.5	Bending	Position 1, Position 2	Yes
7/23	5	17.0	Torsion	Position 1, Position 2	Yes

Table 4.5: Summary of Data Collected

The first three columns show the date of the data set, the length of the run, and the speed of the rotor. The fourth column designates which blade is being excited, the bending or the torsion blade. The fifth column indicates which ECS sensor is taken data. Position 1 corresponds to the ECS mount that holds two sensors (shown in Figure 2.1), and the

66

sensor that is closer to the top of the spin pit. Position 2 corresponds to the ECS that is 90 degrees away from Position 1, in the counter-clockwise direction. Position 1 and Position 2 are at approximately the same chordwise location along the test blade – about 25% of the chord. The sixth column indicates whether or not strain gauge data was being taken.

4.2.2 Verification of Phase of Blade Vibration

In order to detect blade vibrations in the ECS signal, it is necessary to have an independent measurement of the behavior of the blade. Strain gauges were installed on two blades; on one blade they are arranged to sense torsion, and on another they are arranged to sense bending. In Section 3.4, blade vibrations were verified by analyzing the strain gauge data output. To simplify the analysis of the ECS data, it is useful to know if the blade vibrations are synchronous. That is, each time the blade passes an ECS, it is desirable that the same portion of the blade vibration period is taking place. The ECS and strain gauge data taken from the spin pit were analyzed to confirm that the blade vibrations are synchronous.

As discussed in Section 3.4, the strain gauge output from the spin pit can be "ensemble" averaged. In order to average each rotor revolution, a reference point must be chosen. This reference point is determined using the ECS data. Every time a blade passes the ECS, a waveform is produced. The reference point is just the point where the ECS signal first crosses an output value of -0.1 Volts. This can be seen in Figure 4.1. The point where the vertical black line intersects the ECS signal is the chosen reference point. Thus, once a reference point is chosen, a rotor revolution is just the time between two consecutive reference points for the same blade. The ensemble averaging is performed by averaging each of these rotor revolutions.
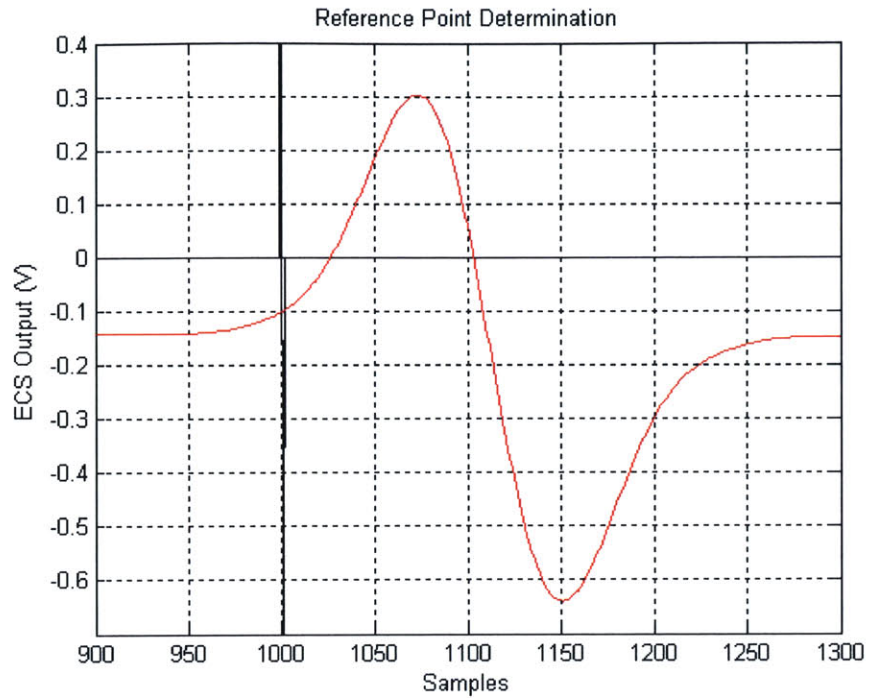
Figure 4.1: Reference Point Determination

This same reference point can be identified in the strain gauge ensemble average, in this case for the bending blade. This is shown in Figure 4.2.
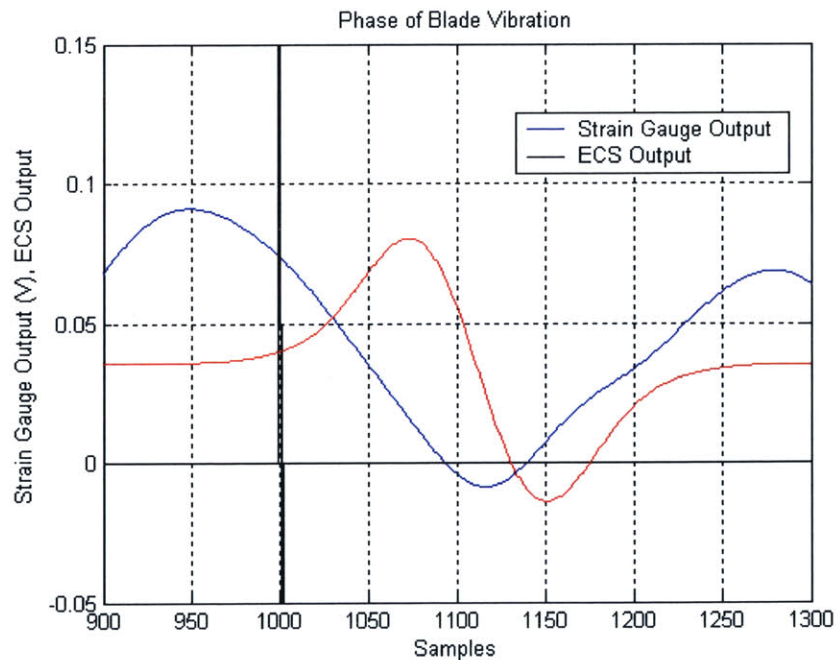
Figure 4.2: Phase of Blade Vibration – Bending Blade

68

The blue line is the ensemble averaged strain gauge data for the bending blade. The red line is the ECS signal, which has been scaled down to fit into the figure. The vertical black line once again indicates the chosen reference point. The point where the vertical black line intersects the strain gauge signal indicates the strain gauge output at the reference point. It can be seen that as the blade passes the ECS, and the ECS signal is produced, the strain gauge output is proceeding from a maximum through a minimum, and then back towards a maximum. Approximately ¾ of a full vibration period takes place during the blade passage. Thus, using this method, the behavior of the bending blade is known as the ECS signal is produced. The strain gauge data indicates where in the vibration period the blade resides during the entire passage across the ECS face. The same effect is seen with the torsion blade, except that the reference corresponds to a different location in the strain gauge output. This is shown in Figure 4.3. For the torsion blade, the reference point corresponds to approximately the maximum of the vibration period.
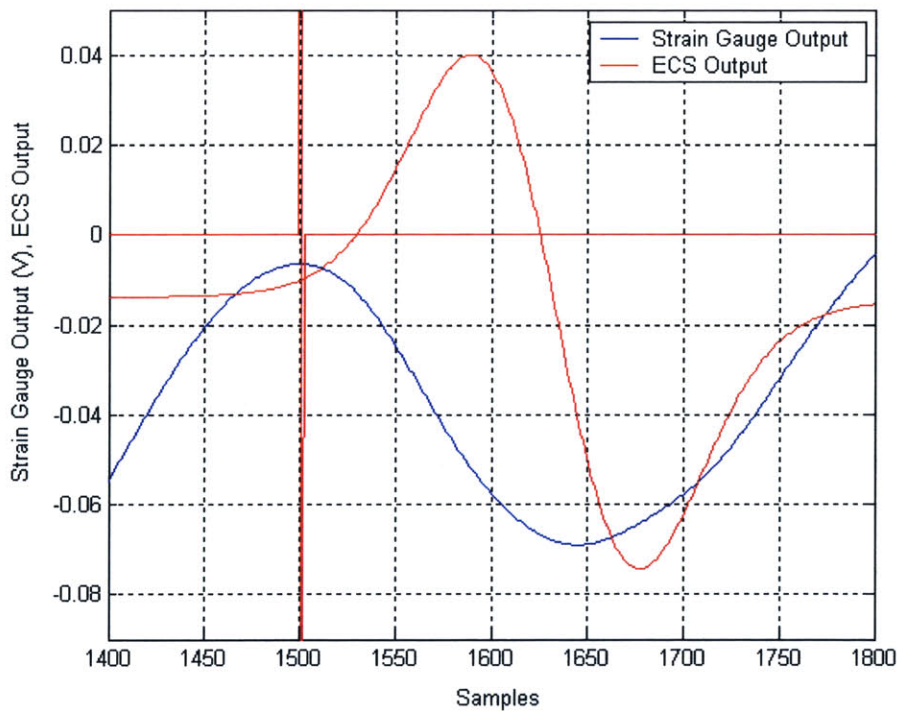
Figure 4.3: Phase of Blade Vibration – Torsion Blade

This result also indicates that the vibration for this data set is synchronous. Each time the blade passes the ECS, a signal is produced which determines a reference point. Therefore, each reference point corresponds to the same circumferential position of the blade in the spin pit. Since the strain gauge data is averaged starting at this point, and since the averaging shows a clear vibration, the vibration must be synchronous. If it were not, then the strain gauge output would be at a different value at each blade passage. That is, when the blade passes the sensor, it would not be at the same point in the vibration period at each passage. Averaging all these different values would produce a result that appeared to be noise, not the clear periodic signal seen in Figure 4.2. Therefore, at each blade passage, the blade vibration must be at the same point in the vibration period, and so the vibrations are synchronous. Moreover, this result is consistent between data sets for both the bending blade and the torsion blade. Several data sets were taken, and plots similar to Figure 4.2 and Figure 4.3 were created for each data set. In each case, the reference point corresponded to the same point in the strain gauge output – about 1/8 of a period beyond the maximum of the strain gauge output for the bending blade, and at the maximum of the strain gauge output for the torsion blade. Thus, the magnets appear to consistently produce a synchronous vibration in the blades.

4.2.3 Evidence of Blade Vibrations in ECS Data

To date, evidence of blade vibrations in the ECS data has not been confirmed. The inability to detect blade vibrations is mainly attributable to the variation in the rotor speed. The motor driving the rotor is unable to rest at a constant speed. Instead, the rotor speed varies by approximately 0.1 Hz, and this variation has created problems for data analysis. However, while no formal algorithms have been developed to deduce blade vibrations from the ECS signal, there are some indications that blade vibrations are affecting the ECS signal. In the future, a better data analysis method could help infer blade vibrations from the ECS signal more systematically. Moreover, Technosciences Inc. is charged with developing more sophisticated algorithms for analyzing the ECS data. All the data taken in the spin pit has been sent to them for their own analysis.

It was decided to examine primarily ECS data from the torsion blade for evidence of blade vibrations. The torsion blade was chosen over the bending blade for several reasons. First, the torsion mode was more consistently excitable in the spin pit. To ensure that a blade was vibrating, a PSD of the strain gauge output was calculated on line using a signal analyzer. The speed of the rotor was adjusted until a large peak appeared at the frequency of the mode of interest. This process was described in Section 3.4, and a sample PSD is shown in Figure 3.16. In general, the torsion blade produced a much more consistent and repeatable peak in the PSD than the bending blade. The peak of the bending blade tended to be half as many dB's in magnitude, and a very precise rotor speed was needed to excite the bending mode. Because the rotor speed varied constantly, this proved difficult, and so generally the bending mode was difficult to excite. One possible explanation for this effect is that the force that the magnets provided on the bending blade was located near a node of the bending mode, and so less excitation of the mode was generated. Regardless, the torsion blade required a less precise rotor speed, and the magnets consistently produced a force on the blade that caused a high strain output at the frequency of the mode. Second, the phase of the torsion mode was extremely convenient for analysis, although this was pure luck. The vibration period of the torsion blade is plotted next to a simultaneous ECS pulse in Figure 4.3. It can be seen clearly that as the blade begins passing the ECS face, and the ECS signal begins, the strain gauge signal is at a maximum. Therefore, the displacement of the blade tip due to the vibration of the mode is at a maximum at this location. This is a convenient occurrence. Through the first half of the blade passage of the ECS, the blade tip is vibrating from a maximum position to a minimum position. In this case, the blade tip is moving in the direction opposite the rotation direction. For the second half of the blade passage, the opposite occurs, as the blade tip moves in the same direction as the rotation direction. In general, the phase of the vibration relative to the passage of the ECS sensor makes it a simple exercise to understand the blade behavior throughout its passage of the ECS. This observation will be discussed in more detail later in this section. Third, eventually the effect of a crack on the test blade was tested. This analysis and testing is described in Section 4.3. The crack was chosen to be a single edge crack. It was hypothesized that a single edge crack, because of its asymmetry, would affect a torsion

71

mode more than a bending mode, due to the asymmetry of a torsion mode. The actual effect of a crack is discussed in Section 4.3. Regardless, the torsion mode seemed more likely to be affected by a crack, and so this was another reason to focus on the torsion blade. In sum, for multiple reasons, the presence of blade vibrations in the ECS signal was examined primarily for the torsion blade.

There are indications that the blade vibrations do in fact affect the ECS signal. The presence of blade vibrations can be seen by plotting the rotation speed of the rotor. The rotation speed is determined by calculating the number of samples between every ECS signal produced by one blade. Because there are three blades spinning at all times, this essentially corresponds to the number of samples between every three ECS signals. The sample that corresponds to the ECS signal is the point where the signal crosses a vertical position of -0.10 V. This reference point was discussed in Section 4.2.2 and an example is shown in Figure 4.1. The rotation speed is calculated by simply dividing the sample rate by the number of samples in one blade revolution, shown in Equation 4.3.

$$Speed = \frac{Sample\_Rate}{\#\_of\_Samples} \qquad \text{Equation 4.3}$$

Thus, the speed of the rotor can be plotted as a function of blade passages for a data set. An example is shown in Figure 4.4. The blue line corresponds to the rotor speed for the run when the magnet arrays are in the spin pit, so that the blade is vibrating. The red line corresponds to the run with no magnet arrays in the spin pit, so that the blade is not vibrating. In Figure 4.4, it can be seen that the non-vibrating speed plot is smoother than the vibrating speed plot. The vibrating speed plot has more choppiness, and a less smooth progression from blade passage to blade passage. This observation is likely an indication of blade vibration. A vibrating blade will tend to arrive at the ECS a little earlier or a little later than a non-vibrating blade, depending on where in the vibration period the blade resides. This inconsistent arrival time could explain the choppiness seen in Figure 4.4.
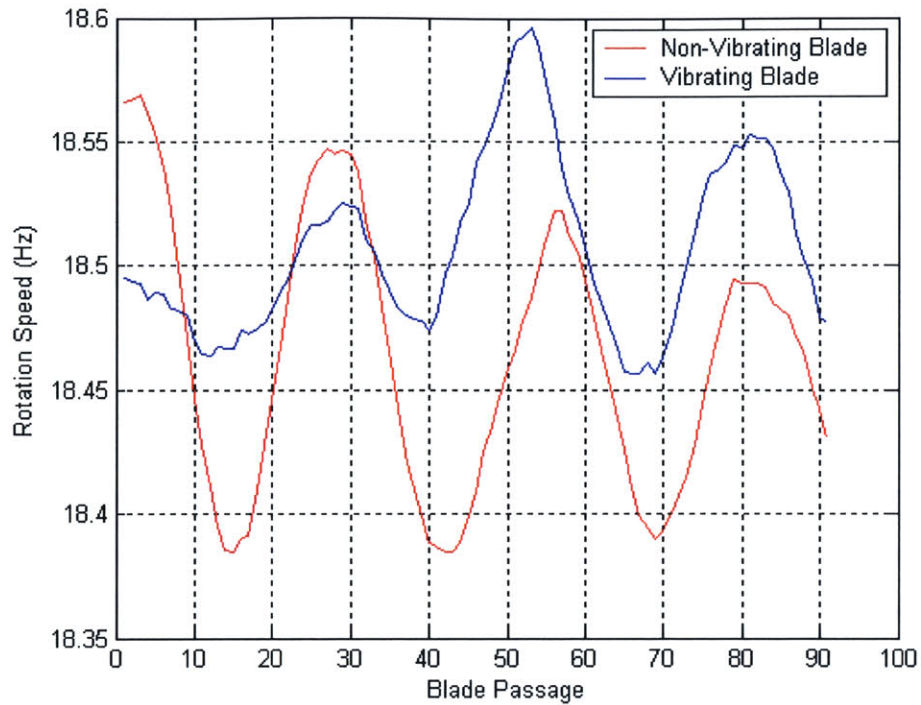
Figure 4.4: Comparison of Rotor Speed for Vibrating and Non-Vibrating Blade

This effect is not consistent with a synchronous vibration however. As was discussed in Section 4.2.2, the blade vibrations are synchronous, and so the blade arrives at the ECS at the same point in its vibration period at every revolution. A synchronous blade vibration should produce an equally smooth speed plot as a non-vibrating blade, because from blade passage to blade passage, the blade is always at the same point in its vibration period. The results of the speed plot shown in Figure 4.4 contradict this fact. However, this same effect was seen in multiple data sets, so it cannot simply be treated as an aberration.

One explanation is that the varying rotor speed affects the vibration amplitude of the blade. The magnets excite the blade at a very precise rotation speed. Small deviations, even 0.2 Hz, will cause the amplitude of the blade vibrations to decrease dramatically. This can easily be seen by plotting a PSD on the signal analyzer, which is described in Section 3.4. If the rotor speed is slightly off the correct rotor speed to cause the blade to vibrate, the amplitude of the peak at the desired frequency will decrease dramatically, by at least 10 dB. Because the rotor speed varies constantly, for certain revolutions, the

magnets will be exciting the blade to a higher degree than during other revolutions. This will cause the vibration amplitude to vary from revolution to revolution. So, even though the blade will be at the same point in the vibration period at each blade passage (because the vibration is synchronous), the blade will arrive at the ECS at slightly different times depending on the amplitude of the blade displacement. This explanation seems to reconcile the seeming contradiction between synchronous vibrations and varying time of arrivals.

As stated above, one reason to focus on data from the torsion blade was the convenient phase of the vibration. The ECS signal begins just as the blade reaches a maximum in it vibrations period, and so there is a clear knowledge of the blade behavior throughout the blade passage. A plot of this occurrence was given in Figure 4.3, and is given again below in Figure 4.5.
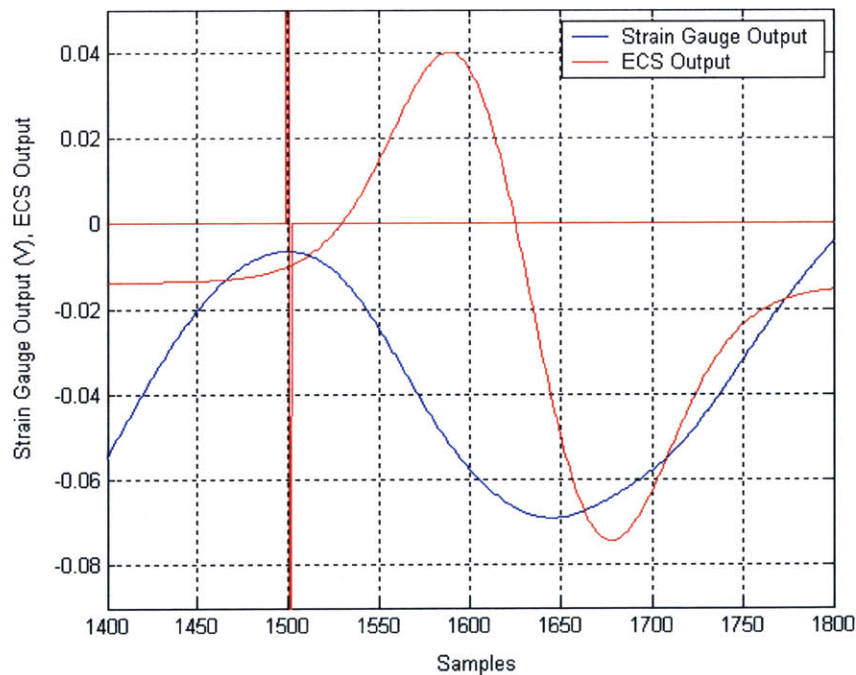
Figure 4.5: Phase of Blade Vibration – Torsion Blade

As a consequence of Figure 4.5, it was hypothesized that blade vibrations should be identifiable in the ECS signal. The reasoning went as follows. When the vibrating blade first begins to pass the ECS face, the displacement of the torsion blade is at a maximum.

Specifically, the blade tip is displaced in the direction of the rotation. As the blade continues to pass the sensor, its vibration continues, and so the blade tip moves in the direction opposite the rotation direction, until it reaches a position where it is maximally displaced in this direction. This occurs at about 50 samples before the ECS signal reaches its minimum point, or at about sample number 1650 in Figure 4.5. So, during approximately the first half of passing the ECS face, or about 150 samples, the vibrating blade tip moves backwards relative to its hub. On the other hand, during the runs when no magnet arrays are installed in the spin pit, the blade is not vibrating. During these runs, when the blade first starts passing the ECS face, the blade tip has almost zero displacement, and does not move at all during the rest of the passage. Therefore, between the point when the blades first start passing the ECS face, and the point where the vibrating blade tip reaches a minimum displacement (maximum in the direction opposite the rotation direction), the vibrating blade tip will tend to lag behind the non-vibrating blade tip. That is, the vibrating blade tip is moving slower than the non-vibrating blade tip during this portion of the blade passage. Therefore, because the ECS produces a signal that is a function of the position of the blade tip, and because the vibrating blade lags the non-vibrating blade during the first half of the blade passage, it seems likely that the ECS signal of the vibrating blade would lag that of the non-vibrating blade, and so be shifted to the right somewhat, during the first half of the blade passage.

A calculation was made to estimate how much the vibrating blade's ECS signal should lag that of the non-vibrating blade. The amplitude of the displacement of the torsion blade was estimated in Section 4.1 to be approximately 0.3 mm. Therefore, during the blade vibration period, the blade tip moves a total of approximately 0.5 mm (because of rounding it is not 0.6 mm). Thus, during the first portion of the blade passage, the blade tip moves from about 0.5 mm in the direction opposite the rotation direction. However, the 0.3 mm estimate for the amplitude of the displacement is for a position at the leading edge of the blade. The ECS is located at a chordwise location of approximately 25%, and so the amplitude of the vibration is lower here. The hammer testing, described in Section 3.1, indicates that the magnitude of the transfer function from strain to blade tip acceleration is approximately half at the chordwise location of the ECS sensor.

Therefore, the blade tip moves approximately 0.3 mm total in the direction opposite the rotation direction, during the first half of the blade passage, and so the vibrating blade is lagging the non-vibrating blade by 0.3 mm at the point that corresponds to the minimum in the vibration amplitude. The time it takes for the blade to travel this extra 0.3 mm should correspond to the amount of time the vibrating blade is lagging by, and therefore the number of samples that the vibrating blade ECS signal is lagging by. To calculate this number of samples, the speed of the blade tip needs to be known. The speed of the blade tip is simply calculated using Equation 4.4.

$$V_{TIP} = f * 2\pi * R_{TIP}$$
Equation 4.4

where: V_{TIP} = velocity of the blade tip

f = rotation speed of the blade, approximately 18 Hz.

R_{TIP} = radius of the blade tip, approximately 9 inches, or 0.23 m.

Therefore, using the values for R_{TIP} and f, the blade tip is traveling at approximately 26.0 m/s. The amount of time the blade takes to travel 0.3 mm at this speed is given in Equation 4.5.

$$t = \frac{D}{V_{TIP}} = \frac{0.0003m}{26\frac{m}{s}} = 1.1 * 10^{-5} s$$
Equation 4.5

This value for t can be converted into samples by multiplying by the sample rate. This is shown in Equation 4.6.

$$\#\_Samples = (1.1 * 10^{-5} s) * \left(400,000 \frac{Samples}{s}\right) \approx 4\_Samples$$
Equation 4.6

Thus, using this argument, it can be hypothesized that the ECS signal of the vibrating blade should be lagging that of the non-vibrating blade by approximately 4 samples by the time the vibrating blade reaches its minimum displacement. To confirm this hypothesis, the ECS signals for the vibrating and non-vibrating blade were plotted, using the common reference point discussed in Section 4.2.2 as the initial point. However, this situation is complicated greatly by the variations in the rotor speed. As stated previously, the rotor speed changes continuously, as shown in Figure 4.4. Moreover, the width of the ECS signal is proportional to the speed of the passing blade. Therefore, the changing

76

rotor speed has the effect of producing ECS signals of varying width. This variation is on the order of 5 samples, and so the ECS signals are spread out enough that any lagging of the vibrating blade due to the blade vibration is masked by the rotor speed variation. To counteract this effect, an interpolation scheme was employed to remove the effect of the rotor variation. Each of the ECS signals for a single blade passage is of different lengths, due to the variable rotor speed. These signals of different lengths were then stretched, using linear interpolation, so that they were all of the same length. In this way, the rotor speed variation was removed, because all of the signals were stretched an amount proportional to their length, which is inversely proportional to the speed of the rotor during that signal. Unfortunately, while this scheme helped reduce the variation in the width of the signal somewhat, it was not effective enough to completely remove the effect of the variable rotor speed. Because of this, the vibrations of the blade are still not identifiable. That is, the poor resolution of the ECS signals, even after interpolation, overwhelms any evidence of the vibrating blade lagging the non-vibrating blade. Thus, while the strain gauge signal confirms that the blade is vibrating, these vibrations do not affect the ECS signal in a way that is detectable using the current data analysis methods.

There are courses of action that may facilitate the detection of vibrations in the ECS signals. First, reducing the rotor speed variations would make the data analysis significantly simpler. The variable speed causes the ECS signals to have varying widths, and this clouds any indication of blade vibrations. Moreover, the interpolation scheme has not been perfected, and it is still insufficient to completely remove the effect of the speed variations. A better interpolation scheme combined with a more constant speed rotor would be much more likely to yield evidence of the blade vibrations. A more consistent rotor speed would have the added effect of allowing the magnets arrays to excite the blade more precisely. That is, speed variations cause the blade to be excited at frequencies that are slightly different from its resonant frequency, and this reduces the amplitude of the vibration. A more consistent speed would result in a more consistent excitation, and therefore a larger amplitude of vibration. A larger vibration amplitude would produce an even greater lag effect in the ECS signals, which would be easier to identify.

In sum, while little evidence of blade vibrations has been identified in the ECS signal to date, in the future it is likely that such vibrations will be evident. First, the strain gauge output on the signal analyzer and the ensemble averaging indicate that the blade is consistently vibrating due to the forcing from the magnet arrays. This forcing is producing a sinusoidal displacement in the tip of the blade, and the magnitude of this displacement can be estimated using the transfer functions developed in Section 3.1. The convenient phase of vibration of the torsion blade, shown in Figure 4.5, should result in the vibrating blade lagging the non-vibrating blade during the first half of the blade passage of the ECS face. The variation of the rotor speed appears to be the source of the problem, by drowning out this effect. While this effect has not been identified, there are several courses of action that would likely reduce the rotor speed variations, and enhance the lag effect in the ECS signals.

4.3 Crack Analysis

Excessive compressor blade vibrations can lead to the formation and growth of high cycle fatigue cracks, as mentioned in Section 1.1.2. These cracks can lead to blade fracture, which could result in a catastrophic failure of a gas turbine engine. Cracks also affect the modes of blades, by reducing their structural stiffness. A hypothesis of this thesis is that vibration sensing of blades can lead to crack detection, by inferring the presence of a crack when the blade mode shape or frequency is changed sufficiently (See Section 1.1.4). To that end, it is necessary to explore this hypothesis, by analyzing and testing the effect of a crack on the mode shape and frequency of a blade.

This section will describe work that was done in order to examine this hypothesis. The goal is to crack the test blade in a "realistic" way, so that it can then be tested in the spin pit rig, and ECS data for a cracked an uncracked test blade can be compared. The term "realistic" means a crack in the test blade that is representative of a crack in an actual operating gas turbine engine. That is, blades in actual gas turbine engines crack in certain locations, and these cracks grow to certain lengths after a number of engine cycles.

These actual cracks will have a certain effect on the resonant frequencies and mode shapes of the actual blades. To be consistent, the crack in the test blade should have a location and size that affects the modes of the test blades to the same extent. Throughout this section, a blade in an actual engine will be used as a baseline for comparison. This blade will be referred to as the "real blade," to distinguish it from the test blade.

4.3.1 Crack Location

Before the effect of a crack can be examined, the location of the crack must first be determined. Cracks will tend to form at locations where sharp edges exist. Sharp edges lead to stress concentration, where the localized stress can be significantly higher than the mean stress outside the vicinity of the sharp edge. The sharp edges can be on both the leading and trailing edges of compressor blades, as well as at locations of foreign object damage or microscopic material defects[13]. This supposition is supported by the work of Professor Ritchie at the University of California, Berkeley. Ritchie explored the growth of high cycle fatigue cracks in gas turbine compressor blades. Many of his tests focused on through thickness cracks, initiating at the edges of material specimens, as well as foreign object damage[14]. For this thesis, the leading and trailing edge of a blade will be chosen as likely places for the initiation of a HCF crack.

HCF cracks grow due to cyclic loading. In engine blades, blade vibrations can generate this loading. When a critical speed is reached, a blade mode is excited and proceeds to vibrate, which stresses the blade. Thus, HCF cracks will tend to grow in regions of high stress due to blade vibrations. That is, regions where an excited blade mode causes high stress levels are likely locations for HCF cracks. For lower order modes, like the first bending mode, and the first torsion and second bending modes shown in Figure 3.10, regions of high stress tend to be near the root of the blade, and near the leading and trailing edges. Moreover, the regions near the root of the blade have the highest centrifugal stresses, which provide a steady-state stress level that contributes to crack growth. The results of the FEM dynamic analysis, described in Section 3.2.2, confirm

these locations of high stresses for the blade modes. The stress levels for the first torsion mode and second bending mode are shown in Figure 4.6.
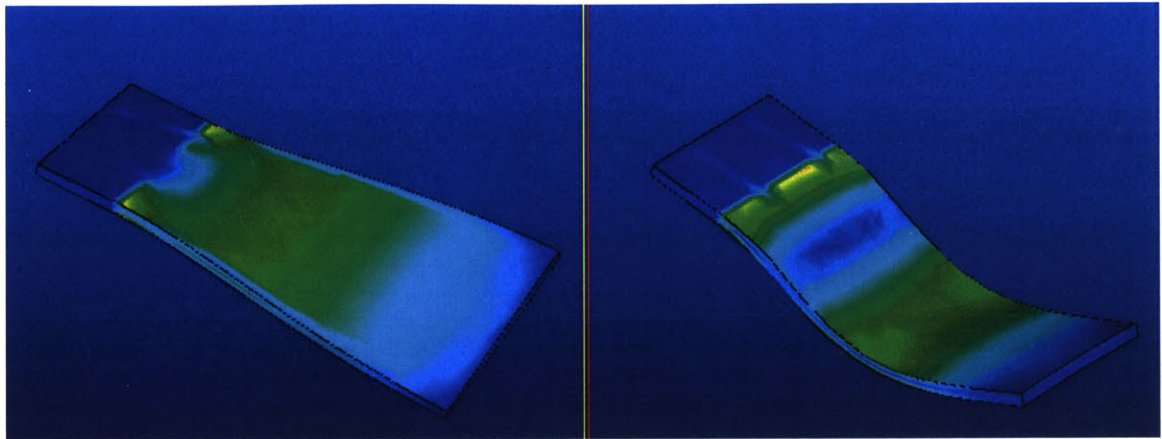
Figure 4.6: Stress Levels for Simplified Blade Modes

These plots of stress show that for the first torsion mode and second bending mode of the simplified blade, the regions near the root and edges are the regions of highest stress.

In sum, HCF cracks tend to initiate in region of stress concentration near the blade edges. HCF cracks grow due to cyclic stresses, which are generated by blade vibrations. The regions of highest stress for the low order blade modes tend to be near the root and edges of the blade, which is also where the centrifugal stress is greatest. These regions of high stress will cause high cycle fatigue cracks to grow. Thus, the crack in the test blade should be located near the root and edges.

4.3.2 Critical Crack Length Estimation

Next, the critical crack length of the real blade was determined. The critical crack length is defined such that for a given stress level, material, and blade geometry, a crack with length equal to the critical length will cause rapid crack propagation, and therefore fracture. Thus, the critical crack length can be thought of as the maximum allowable crack size in a compressor blade. In order to determine the critical crack length in the real blade, the stress level must first be determined. A simplified centrifugal stress model was used to estimate the stress level in the real blade. Vibratory stresses were ignored for

the sake of simplicity. The centrifugal stress was calculated by treating the blade as a constant cross sectional area bar rotating about an axis at some angular velocity. The equation for the centrifugal stress at some radius r is:

$$\sigma = \int_r^{r_T} \rho \omega^2 r dr = \left(\frac{\rho \omega^2}{2}\right)\left(r_T^2 - r^2\right)$$

<div align="right">Equation 4.7</div>

where: σ = stress at some radius r

ρ = material density

ω = angular velocity of rotating blade

r_T = radius of blade tip

The fan blade from the CFM 56-3 engine was chosen as a representative real blade. The material of the blade is Ti 6Al-4V. Some relevant material properties and geometry are given in Table 4.6.

Tip Radius (m)	.64
Root Radius (m)	.17
Density (m/kg^3)	4400
Plane Strain Fracture Toughness (MPa*m^.5)	100

<div align="center">Table 4.6: Some Properties of the Real Blade</div>

The root radius is the radius of the root of the blade, where the centrifugal stress will be a maximum. The angular velocity ω was calculated by assuming that the tip Mach number of the blade is equal to one. This is a reasonable assumption for modern gas turbine engines. Therefore the angular velocity can be calculated using Equation 4.8.

$$\omega = \frac{speed\_of\_sound}{r_T} = \frac{343\frac{m}{s}}{.64m} = 540\frac{1}{s}$$

<div align="right">Equation 4.8</div>

Using these values for r, r_T, ω, and ρ, the centrifugal stress at the blade root can be calculated using Equation 4.7. The result is an estimate of stress of $\sigma = 500MPa$. Because of the many simplifications made to calculate this value for stress, a margin of safety of 20% was employed. Also, this estimate only considers centrifugal stress, and

does not take into account the stress generated by vibrations. Therefore, in calculating the critical crack length of the real blade, a value of stress of $\sigma = 600 MPa$ will be used.

If a condition of plane strain is assumed, then the critical crack length can be calculated, using Equation 4.9[1].

$$a_C = \frac{1}{\pi}\left(\frac{K_{IC}}{Y\sigma}\right)^2$$

Equation 4.9

where: K_{IC} = plane strain fracture toughness (given in Table 4.6)

σ = stress calculated = 600 MPa

Y = geometric property = 1.12 (for edge crack)

Thus, using Equation 4.9, the critical crack length can be estimated to be a_C =10 mm. This value is the estimate of the critical crack length for the real blade, which has geometry and material properties based on a fan blade in an actual engine. This estimate is meant to be realistic, in the sense that it approximates what the actual critical crack length would be in a fan blade in an actual gas turbine engine. However, this value for the critical crack length is not the appropriate size for the crack in the test blade. Because the test blade is smaller, the crack in the test blade must be scaled. This scaling will be based on the effect of the crack on the mode of the blade. That is, the crack in the test blade will be scaled to such a size that it has the same percentage effect on the mode of the test blade as the 10 mm critical crack has on the real blade. In order to perform this scaling, an estimate of the effect of a crack on a mode must be performed. This will be done in Section 4.3.3. Once this estimate is complete, then the scaling can be performed to determine the crack length for the test blade.

4.3.3 Estimate of Crack Effect of Mode

A crack in a structure reduces its structural stiffness, causing its resonant frequencies to decrease. A simple example of this effect is a guitar string. A string that is stretched very tightly will have a higher resonant frequency than a string stretched fairly loosely. Intuitively, stiff structures have higher frequency modes than compliant structures, and

82

since a crack reduces structural stiffness, the resonance frequencies of a cracked structure should be lower than an uncracked structure. For a cantilevered beam, which is a good model of a compressor blade, the frequencies of the structural modes are proportional to the square root of the structural stiffness of the beam[15]. This relationship is given in Equation 4.10.

$$\omega_n \propto \sqrt{EI}$$

Equation 4.10

where: ω_n = frequency of mode of order n

E = Young's modulus

I = bending moment of inertia

The profile for the real and test blade will be modeled as a simple diamond shape with chord c and thickness t, shown in Figure 4.7.
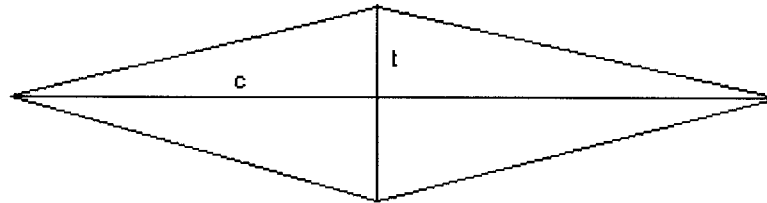
Figure 4.7: Model Blade Profile with No Crack

The moment or inertia of this profile is given in Equation 4.11.

$$I = \frac{1}{48} ct^3$$

Equation 4.11

The effect of the crack is estimated by modeling the crack as removing material from this profile at one spanwise location. That is, the crack of length 'a' removes material from the blade profile, shown in Figure 4.8, which decreases the moment of inertia of the blade at this location.
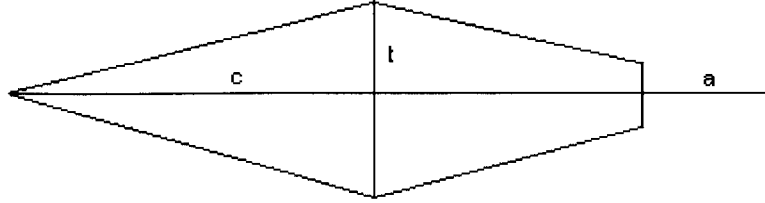
Figure 4.8: Model Blade Profile with Crack

The moment of inertia for the cracked blade profile is given in Equation 4.12.

$$I = \frac{1}{48}ct^3\left(1 - 8\frac{a^4}{c^4}\right)$$

Equation 4.12

Thus, as the crack increases in length, the moment of inertia decreases, causing the resonant frequency to decrease. The percentage change in the resonant frequency of a structure due to a crack is given in Equation 4.13.

$$\%change = 1 - \frac{\omega\_cracked}{\omega\_uncracked} = 1 - \sqrt{\frac{I\_cracked}{I\_uncracked}} = 1 - \sqrt{\left(1 - 8\frac{a^4}{c^4}\right)}$$

Equation 4.13

Thus, using Equation 4.13, the effect of a crack the resonant frequency of a blade mode can be estimated for a given crack length and blade geometry.

4.3.4 Crack Length Scaling

The critical crack length for a real blade, based on the stress levels and geometry of a blade in a real engine, was calculated in Section 4.3.2. The critical crack length was estimated to be 10 mm. In Section 4.3.3, the effect of a crack on the resonant frequency of a structure was estimated. The result is given in Equation 4.13, which gives the percentage change in the resonant frequencies as a function of the crack length and blade geometry. Thus, the effect of a critical crack on the real blade can be estimated. In order to determine the appropriate size of the crack for the test blade, the crack length must be scaled so that the test blade crack has the same effect on the mode of the test blade as the critical crack length has on the real blade. The chords of both blades are given in Table 4.7.

Real Blade Chord (m)	.171
Test Blade Chord (m)	.051

Table 4.7: Chord Lengths of Real and Test Blades

Using, the chord length given in Table 4.7 and the critical crack length of 10 mm, the effect of a crack on the real blade can be calculated using Equation 4.13.

$$\%change = 1 - \sqrt{\left(1 - 8\frac{a^4}{c^4}\right)} = .005\%$$

Equation 4.13

Because the test blade has a different chord length, a different crack length will cause the same change in the resonant frequency of the test blade. While the test blade and real blade are different materials, this change in material is irrelevant in the scaling. This is because the material properties are constant for a given blade, whether the blade is cracked or not. This is clear from Equation 4.13, which shows that the change in the mode is dependent only on the crack length and blade chord. When scaling from the real blade to the test blade, only the percent change in the resonant frequency for the real blade is relevant to the calculation for the test blade. Thus, material properties do no affect the crack length scaling. Again using Equation 4.13, the crack length for the test blade can be calculated.

$$a\_testblade = .005m = 5mm$$

This result gives the crack length of the test blade. A crack of this length changes the mode of the test blade by the same amount that the critical crack of the real blade changes the mode of the real blade. The scaling was performed by modeling the blade as a beam and the crack as a reduction in the moment of inertia of the beam.

Using this method, the effect of a 5 mm crack on the test blade is a reduction in the resonant frequency of only .005%. This is clearly a very small effect. However, the method used to model the effect of a crack is very crude, and shouldn't be viewed as an exact means of determining the relationship between a crack and a structural mode. Its utility lies in its ability to scale crack length with blade geometry. This method allowed for the calculation of an appropriate crack length for the test blade of 5 mm. A crack of

this length can then be generated in the test blade, and its effect on the mode of the blade can be determined experimentally. This will be done in later sections.

4.3.5 Numerical Estimate of Crack Effect

The effect of a crack on the test blade was also estimated numerically using "Pro-Mechanica." A crack of length 5 mm was inserted into the simplified blade model described in Section 3.2. A picture of the blade with the crack is shown in Figure 4.9. The crack is positioned near the root and the leading edge of the blade, as described in Section 4.3.1, and is 5 mm long.
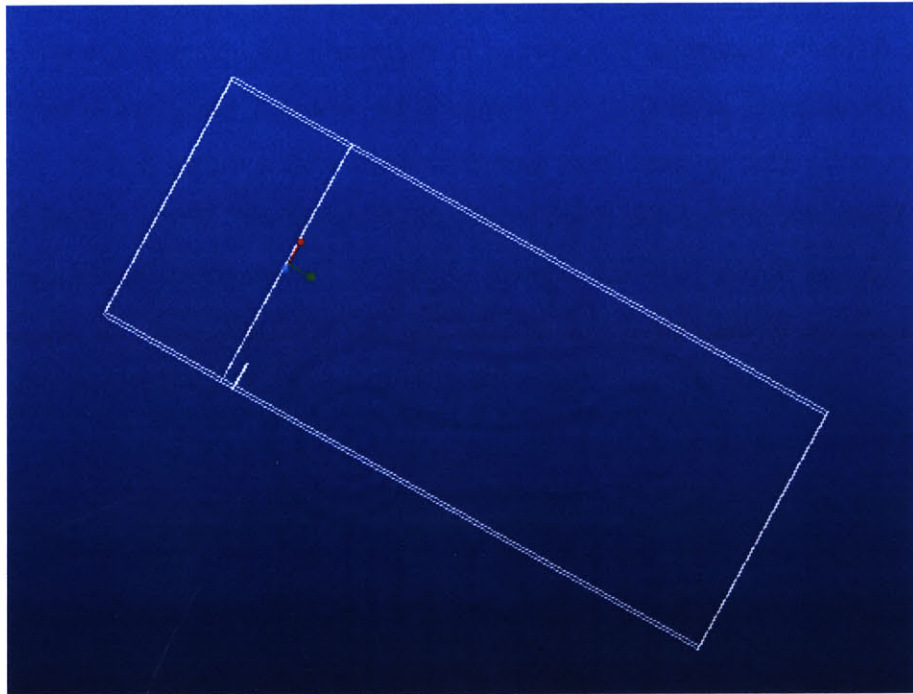

Figure 4.9: Simplified Blade Model with Crack

A dynamic analysis was performed in Pro-Mechanica on the cracked blade. The dynamic analysis was identical to that described in Section 3.2.2, which determined the mode shapes and resonant frequencies of the simple blade model. The results of the analysis are given in Table 4.8.

Mode Type	Frequency – No Crack	Frequency - Crack	% Change
Torsion – Mode 2	1077 Hz	1062	1.4
Bending – Mode 3	1601 Hz	1585	1.0

Table 4.8: Pro-Mechanica Results for Crack Effect

The results of the dynamic analysis of the cracked blade indicated that the resonant frequencies of the cracked blade decreased, as expected. The frequency of the torsion mode decreased by 1.4%, and the second bending mode decreased by 1.0%. These results are in contrast to the results from Section 4.3.4, which indicated that a 5 mm crack would only decrease the blade resonant frequencies by about .005%. However, the methods used to analyze the presence of a crack in Section 4.3.3 were simplistic and only beneficial for scaling. These results from Pro-Mechanica are encouraging. They indicate that a 5 mm crack will have an approximate effect on the modal frequencies of 1 %. During force hammer testing, described in Section 3.1, the signal analyzer was used to generate frequency response functions between the hammer and the accelerometer, and the hammer and the strain gauges. The resolution on the signal analyzer was approximately 2 Hz. For these frequency response functions, so a change in the resonant frequencies on the order of 15 Hz may be detectable using force hammer testing. However, the model used in the dynamic analysis has a greatly simplified cross section and constraints. The effect of an actual crack in the test blade may be less than is indicated by the dynamic analysis. Only with experimental testing of an actual cracked blade can the effect of a crack be truly determined. This will be discussed in Section 4.3.7.

4.3.6 Crack Generation

With the crack location and crack length determined, a crack can be generated in the test blade. Two methods were used to generate the crack. The first was a rough-cut method. A small saw, .01 inches thick, was used to cut the blade near the root of the blade, and at one of the edges. This method was used for its simplicity and rapidity. The cut was 5 mm deep, which is the appropriate length of a crack calculated in Section 4.3.4. This cut

was meant to simulate a crack, and provided a quick way of testing a blade that represented a cracked blade.

The second method to crack the blade will involve cyclic loading that will more closely approximate crack generation and growth in a gas turbine engine. As discussed in Section 1.1.2, HCF cracks have distinct steps. First, as a material is cyclically loaded, a crack is initiated at a point of high stress concentration. Next, the crack propagates, advancing incrementally with each loading cycle. Finally, when the crack has reached its critical size, it grows rapidly and the material specimen fractures. A second test blade will be cracked in such a way as to mimic this process. To date, the second test blade has not been cracked. However, an analysis was performed to estimate the number of cycles and the amount of time required to generate a crack. The analysis proceeds as follows. The crack will be located in the same location as the rough-cut crack described above – at one edge of the blade, near the root. A small initiation site will be created, possibly using a sharp cutting tool, or perhaps spark erosion. This initiation site is intended to model the crack initiation process that is the first step in HCF crack growth. The initiation site is a region of high stress concentration, perhaps near an edge, a location of foreign object damage, or a material flaw. The size of the initiation crack will be 2 mm. This length is based on the work of Ritchie[14], who used 2 mm notches as crack initiation sites in his work. Next, an "Instron" tensile machine will be used to cyclically load the blade in tension. The blade will be clamped in the machine, which provides a tensile stress to the blade that varies sinusoidally in amplitude. This cyclic loading will simulate cyclic vibratory stresses seen by a blade in an engine. As the blade is loaded, the crack will begin to grow from the initiation site until it reaches a length of 5 mm. The crack growth rate can be expressed using the Paris Law. The rate of increase of the crack length a, per cycle N, is given in Equation 4.14[1].

$$\frac{da}{dN} = A(\Delta K)^M \qquad \text{Equation 4.14}$$

A and M are material constants of aluminum, and ΔK is the stress intensity range at the crack tip, and is expressed in Equation 4.15[1].

$$\Delta K = Y(\sigma_{MAX} - \sigma_{MIN})\sqrt{\pi a}$$ Equation 4.15

where: Y = geometric property = 1.12 (for edge crack)

σ_{MAX} = maximum of cyclic stress amplitude = 150 MPa

σ_{MIN} = minimum of cyclic stress amplitude = 4 MPa

The stress levels are based on the capabilities of the "Instron" machine. The total number of cycles needed to generate the crack can be found using Equation 4.16 and Equation 4.17[1].

$$dN = \frac{da}{A(\Delta K)^M}$$ Equation 4.16

This can be integrated from the initial crack length, a_i (2 mm), to the final crack length, a_F (5 mm), shown in Equation 4.17[1].

$$N_{Total} = \int_0^{N_{Total}} dN = \int_{a_i}^{a_F} \frac{da}{A(\Delta K)^M} = \int_{a_i}^{a_F} \frac{da}{A(Y(\sigma_{MAX} - \sigma_{MIN})\sqrt{\pi a})^M} \approx 230,000 \, Cycles$$ Equation 4.17

Thus, it will take approximately 230,000 cycles under these load conditions to grow the crack from the initiation length to the final length. The "Instron" machine operates at a frequency of approximately 8 Hz, so it should take about 8 hours to complete the process of growing the crack to 5 mm. Using this method, a 5 mm crack will be generated in the blade in a way that approximates cyclic loading that a blade undergoes in an engine.

4.3.7   Force Hammer Testing for Crack Analysis

The effect of a crack on a blade mode was estimated both analytically and numerically in Section 4.3.4 and Section 4.3.5, respectively. The results varied considerably, as the analytic result yielded an estimate significantly smaller than the numerical result. Both of these methods have drawbacks, and so force hammer testing was utilized in order to determine the actual effect of a crack on the test blade.

The torsion blade was used for this analysis. It was hypothesized that an edge crack would have a greater effect on a torsion mode than a bending mode. This is because for a

torsion mode, at a spanwise position near the root, the highest stresses occur near the edges, where an edge crack resides. For a bending mode, the stress is essentially uniform at one spanwise location, not depending on the chord position. The results of the numerical analysis, shown in Table 4.8, supported this hypothesis. Thus, the torsion blade was cut with a small saw, described in Section 4.3.6, to simulate a crack. The cut actually made to be 10 mm long instead of 5mm. This analysis is mostly a demonstration that a crack affects a mode, and so a larger crack was used because the effect would be greater, and easier to detect. In the future, when a crack is generated more realistically using the cyclic loading described in Section 4.3.6, it will only be grown to 5 mm, which is consistent with the scaling performed in Section 4.3.4.

A force hammer test was performed in order to determine the effect of the 10 mm cut on the blade modes. The test was essentially identical to the force hammer testing described in Section 3.1. First, five frequency response functions between the hammer and the tip acceleration were created, using the accelerometer positioned at one location near the root of the blade, and hitting the blade at five tip positions with the hammer. Next, a frequency response function between the hammer and the strain gauges was created, as the blade was struck by the hammer at the position where the accelerometer used to be located. Lastly, each of the five hammer to accelerometer frequency response functions were divided by the hammer to strain gauge frequency response function, yielding a transfer function between strain and tip acceleration. Overall, this procedure is identical to that described in Section 3.1.

The results of the force hammer test indicate some evidence that the crack has affected the torsion mode of the test blade. First, the resonant frequency of the torsion mode has decreased from 1176 Hz to 1174 Hz. While this is a small change, it is consistent. Three identical hammer tests were performed on the cracked test blade, and all three revealed this slight decrease in the resonant frequency of the torsion mode. Moreover, this decrease in frequency appears in both the accelerometer and strain gauge tests. For both, the peak of the torsion mode frequency response function has shifted downwards to 1174 Hz. While this change is indeed slight, its consistent with the hypothesis that a crack will

decrease a the resonant frequency of a blade by reducing its structural stiffness. This hypothesis was born out to varying degrees in the analysis described in Section 4.3.4 and Section 4.3.5. A decrease in frequency of 2 Hz corresponds to a percentage change of approximately .2%. This result is larger than the estimate of .005% from Section 4.3.4, but smaller than the 1.4% estimate from the numerical analysis in Section 4.3.5.

The mode shape of the blade also appears to have changed slightly due to the presence of the crack. This change can be seen by looking at the final transfer functions between strain and blade tip acceleration. The magnitude of the transfer functions at the frequency of the torsion mode is the relevant parameter. This can be found by merely taking the absolute value of the five transfer functions at 1176 Hz for the uncracked blade, and 1174 Hz for the cracked blade. These values can then be plotted and compared to determine the effect of the crack. The results are shown in Figure 4.10.
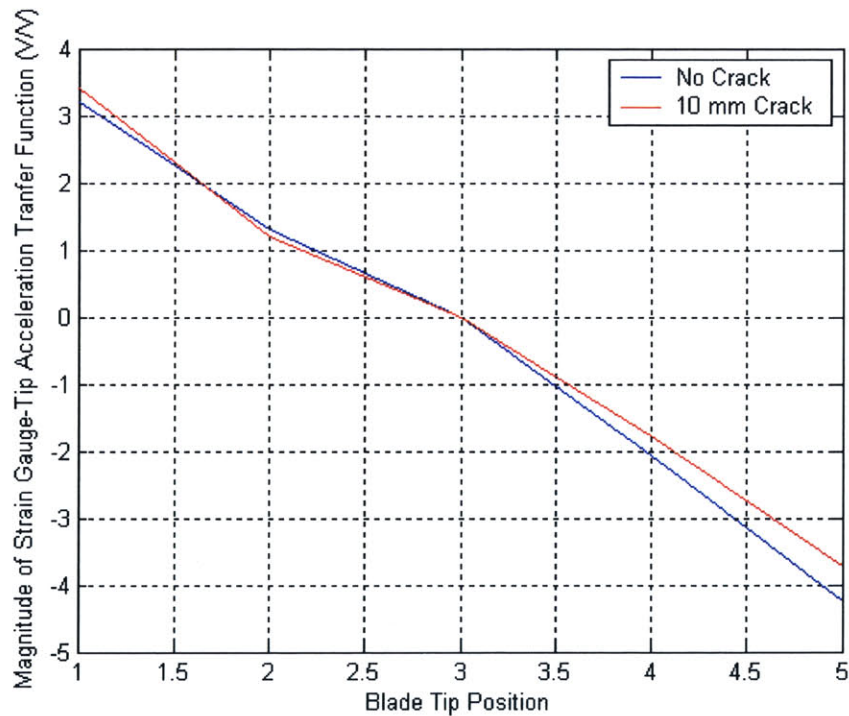

Figure 4.10: Comparison of Cracked and Uncracked Blade Transfer Functions

The blue line corresponds to the blade before it was cracked, and the red line corresponds to the cracked blade. The x-axis is the blade tip position, where position 1 is very near one edge, and each other position is 0.5 inches farther along the chord at the blade tip.

91

Thus, position 3 is at the half-chord position, and position 5 is at the other edge. The cracked blade transfer function is actually the average of three separate hammer tests all performed on the blade with the 10 mm cut. All three exhibited the same qualitative behavior. The relative phase of the blade tip positions is imposed in order to emphasize the fact that this mode is a torsion mode. That is, while the magnitude of each transfer function is positive, the values at position 4 and position 5 are made negative. This serves to emphasize the fact that this is a torsion mode, and to clarify the presence of asymmetry in the crack effect. The presence of the crack seems to have an asymmetric effect on the blade mode shape. Position 1 has a slightly higher magnitude (about 6%), while position 5 has a lower magnitude (about 13 %). This asymmetry is encouraging. The crack is a single edge crack, so it is likely that it would affect the two edges differently.

Overall, the crack seems to have a small but noticeable effect on the mode of the torsion blade. The resonant frequency of the torsion mode is reduced by 2 Hz, and the mode shape changes asymmetrically. These changes are consistent, as three separate hammer tests produce similar results.

5 Conclusions

This thesis aimed to develop the ability to test eddy current sensors in a simulated gas turbine environment. The experiments were performed in a spin pit rig, in the Gas Turbine Lab at MIT. The goals of this research, and the important questions to be answered, were laid out in Section 1.2.3. To date, many of the questions have been answered, and the capabilities are in place for future work. Several concluding remarks can be made from the research performed in this thesis.

1. The experimental setup in the spin pit rig has been completed. The capability is in place to take ECS data for a passing blade in the spin pit. Also, magnet arrays can be used to provide an excitation force on the spinning blades at a desired frequency. Strain gauges have been attached to some of the blades, and the strain gauge output can be used to independently measure blade vibrations. Finally, a procedure for dynamically balancing the spin pit rotor has been developed and its effectiveness has been verified.

2. Force hammer testing was used to determine the resonant frequencies and mode shapes of the test blades. The test blades each had a first torsion mode and a second bending mode in the 1.1-1.3 kHz range. The force hammer testing was also used to compute transfer functions between the strain gauges and the blade tip acceleration. This provided independent knowledge of the blade tip behavior using just the strain gauge output. Using these transfer functions, the amplitude of the displacement of the vibrating blades can be estimated for a blade that is spinning in the rig.

3. Pro Mechanica was used to perform an FEM analysis on a simplified model of the test blade. The results confirmed the mode shapes determined with the force hammer testing, and gave a qualitative confirmation of the resonant frequencies.

4. An analysis was performed to understand how a crack would affect a blade. The analysis began by determining the likely location and size of a crack in a compressor

blade in an actual gas turbine engine. Next, an estimate of the effect of a crack on a blade mode was made. This estimate was used to scale the crack size from a real blade to the test blade used in the spin pit. A crack length of 5 mm was chosen for the test blade. This analysis predicted a negligible change in the blade mode due to the crack. However, FEA analysis was performed in Pro Mechanica on a cracked blade, and this analysis provided a more substantial estimate of the effect of a crack on a blade mode. A 10 mm crack was created in an actual blade by simply cutting the blade with a narrow saw. A crack will be generated in a second blade using the more realistic technique of cyclic loading. The cyclic loading will be carried out using a tensile machine, and an analysis was performed to estimate the total number of cycles needed to generate the 5 mm crack using this machine. Finally, force hammer testing was used to experimentally determine the effect of a crack on the test blade. The cracked blade was found to have a slightly lower resonant frequency – about 0.2%. The transfer function from the strain gauges to the tip acceleration also changed due to the presence of the crack. Thus, a crack does indeed seem to change the mode of a blade.

5. Several data sets were compiled from spin pit testing. Each data set corresponded to data for either the "torsion blade" or the "bending blade," so called for their respective strain gauge instrumentation setups. The rotor speed was such that the magnet arrays either excited the torsion mode of the torsion blade, or the bending mode of the bending blade. Within each data set, two actual runs were performed. For one run, the magnet arrays were installed in the spin pit to provide an excitation force on the blade. For the second run, the magnet arrays were removed. In this way, one run consisted of data for a vibrating blade, and one run did not. For each run, ECS data was taken, and strain gauge data was also often taken. Thus, there are numerous data sets that consist of ECS data for vibrating and non-vibrating passing blades, for both the torsion and the bending blade.

6. To date, blade vibrations have not been conclusively detected in the ECS signals. Some indication of blade vibrations can be seen by plotting the speed of the rotor for

the vibrating and no vibrating case. However, the blade vibrations have not affected the ECS signal in a way that is consistently identifiable with the current analysis methods. It was believed that the tip of the vibrating blade would lag behind the non-vibrating blade tip for the torsion blade. A calculation was performed that estimated that the vibrating ECS signal would lag the non-vibrating ECS signal by approximately 4 samples. To date, this lag effect has no been identified. The main hindrance to the analysis is the inconsistency of the rotor speed. This variation causes ECS signals of varying width, which likely masks any evidence of the vibrating blade lagging. An interpolation scheme was used to remove the effect of the varying rotor speed, but so far, it has not helped to yield evidence of blade vibrations. Several steps can be taken to increase the likelihood of identifying blade vibrations in the ECS signal. These recommendations will be listed in Section 5.1.

5.1 Recommendations

At the end of Section 4.2.3, several courses of action were mentioned that could improve the process of vibration sensing in the ECS signal. These recommendations, as well as some others, are given here.

1. Reducing the variation in the rotor speed is likely to greatly facilitate data analysis. The varying speed produces ECS signals of varying width, and this hinders our ability to identify blade vibrations in the ECS signals. Reducing the rotor speed variation would have the added benefit of producing higher amplitude blade vibrations, by allowing the magnet arrays to excite the blade more precisely. Larger blade tip displacements due to vibrations should have a greater effect on the ECS signals.

2. There are two compelling reasons to focus on the bending blade over the torsion blade. First, the amplitude of vibration is constant along the chord of the blade tip, so the positioning of the ECS is irrelevant. Second, as calculated in Section 4.1, the amplitude of vibration of the bending blade is about twice that of the torsion blade. However, the torsion blade was chosen for several reasons, mentioned in Section

4.2.3. The most important was the consistency of the vibration of the torsion blade. The PSD of the strain gauge output was significantly more consistent for the torsion blade. The bending blade excitation was much more sensitive to speed variations, and given the unsteadiness of the rotor speed, this resulted in inconsistent blade excitation. It was hypothesized in Section 4.2.3 that the magnet arrays are producing a force on the bending blade that is located near a node of the bending mode. This could result in smaller amount of blade excitation. To investigate this hypothesis, the mode shape of the edge of the blade should be determined. The mode shape of the blade tip was determined using the force hammer and accelerometer, as described in Section 3.1. A similar test should be carried out on the blade edge. The edge should be struck at several spanwise locations, and a mode shape for the bending mode determined. If the magnet arrays' locations were near one of the nodes of the edge mode shape, this would confirm the hypothesis. This effect could be eliminated by moving the magnet arrays to a radial position that corresponds to a larger amplitude of the edge mode shape. This would produce a greater response from the blade, and therefore a larger and more consistent blade vibration. In this way, the bending blade could be used to identify vibrations in the ECS signal, along with the torsion blade.

References

1. William D. Callister, J., *Material Science and Engineering; An Introduction.* 2000. **Fifth Edition**: p. 213.
2. Epstein, A.H., *Aeromechanics Lecture; 16.511.* 2004: p. 2.
3. Techno-Sciences, I., *Minimal Sensor Signal Processing for Turbine Engine Health Monitoring.* 2002: p. 4.
4. Kerrebrock, J.L., *Aircraft Engines and Gas Turbines.* 1992. **Second Edition**: p. 332.
5. Wayne C. Haase, J.K.R., *Detection and Characterization of Blade/Disk Cracks in Operational Turbine Engines.* p. 2.
6. Instruments, T., *High Common-Mode Voltage DIFFERENCE AMPLIFIER.*
7. Measurements Group, I., *2310 Instruction Manual.* p. 17.
8. Corporation, K.I., *Model 9722A Manual.*
9. Harris, C.M., *Shock and Vibration Handbook.* 1996. **4th Edition**: p. 10.8.
10. Strang, G., *Introduction to Applied Mathematics.* 1986.
11. Toogood, R., *Pro/Mechanica Tutorial Structure.* 2001.
12. Moaveni, S., *Finite Element Analysis.* 2003. **Second Edition**.
13. MURI, H., *Program Goals.*
14. Ritchie, R.O., *Mixed-Mode, High-Cycle Fatigue-Crack Growth Thresholds in Ti-6Al-4V: A Comparison of Large and Small Crack Behavior.*
15. Bismarck-Nasr, M.N., *Structural Dynamics in Aeronautical Engineering.* 1999.